Materials & Design 223 (2022) 111136

Contents lists available at ScienceDirect

Materials & Design

journal homepage: www.elsevier.com/locate/matdes

Interface mediated deformation and fracture of an elastic–plastic bimaterial system resolved by *in situ* transmission scanning electron microscopy

Markus Alfreider [a,b,*], Glenn Balbus [b], Fulin Wang [b], Johannes Zechner [c], Daniel S. Gianola [b], Daniel Kiener [a]

[a] Department Materials Science, Chair of Materials Physics, Montanuniversität Leoben, 8700 Leoben, Austria
[b] Materials Department, University of California, Santa Barbara, CA 93106, USA
[c] KAI Kompetenzzentrum Automobil- und Industrieelektronik GmbH, Villach, Austria

HIGHLIGHTS

- A novel push-to-shear testing configuration for *in situ* transmission scanning electron microscopy is introduced.
- The failure behaviour of a highly ductile microscale Cu-WTi interface upon mode I or mode II loading are experimentally determined.
- Characteristics changed from void nucleation and coalescence (mode I) to nucleation and propagation of an interface crack (mode II).
- Dislocation dynamics and crack propagation combined with theoretical considerations serve to obtain failure parameter estimates.

ARTICLE INFO

Article history:
Received 17 June 2022
Revised 10 August 2022
Accepted 8 September 2022
Available online 14 September 2022

Keywords:
Mode mixity
Interface toughness
Thin films
Crack extension
TSEM

GRAPHICAL ABSTRACT

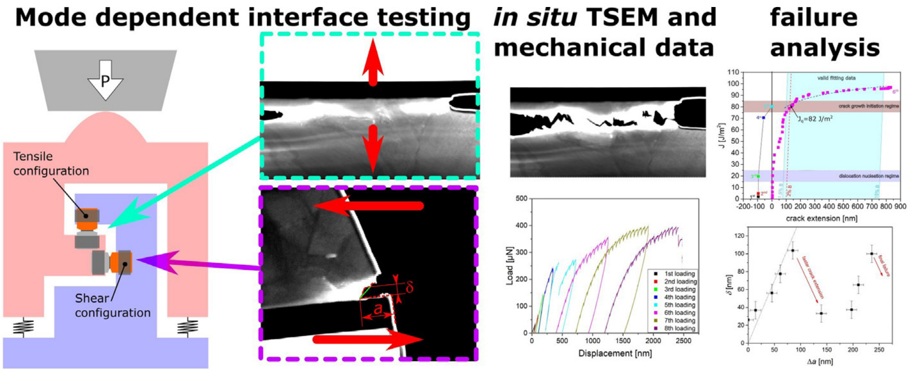

ABSTRACT

A wide variety of today's engineering material systems consist of multiple layered constituents to satisfy varying demands, *e.g.* thermal barrier- or hard coatings, thermal- or electrical conduction or insulation layers, or diffusion barriers. However, these layers are commonly only of the order of a few hundred nanometers to microns thick, which renders conventional mechanical investigation of interfacial failure quite challenging, especially if plastically deforming constituents are involved. Herein, we present an *in situ* study of the mechanical deformation of a WTi-Cu model interface, commonly encountered in the microelectronics industry, utilizing transmission scanning electron microscopy. This approach elucidated the interplay between plastic deformation and fracture processes when loading either perpendicular (mode I) or parallel to the interface (mode II). Under mode I purely ductile failure in the Cu phase, exhibiting dislocation slip facilitated void nucleation and coalescence, was observed with an initiation value for dislocation propagation of $J_{\mathrm{dislocation}} \approx 15$ J/m^2. Mode II loading exhibited nucleation and propagation of an interface crack, with the initiation value for crack extension as $J_{\mathrm{crack}} \approx 8.8$ J/m^2. The results are discussed with respect to the frameworks of classical fracture mechanics and dislocation plasticity, providing fundamental insight into the failure behaviour of elastic–plastic interfaces with respect to loading orientation.
© 2022 The Authors. Published by Elsevier Ltd. This is an open access article under the CC BY license (http://creativecommons.org/licenses/by/4.0/).

---

* Corresponding author at: Department Materials Science, Chair of Materials Physics, Montanuniversität Leoben, 8700 Leoben, Austria.
E-mail address: markus.alfreider@unileoben.ac.at (M. Alfreider).

https://doi.org/10.1016/j.matdes.2022.111136
0264-1275/© 2022 The Authors. Published by Elsevier Ltd.
This is an open access article under the CC BY license (http://creativecommons.org/licenses/by/4.0/).

1. Introduction

The heterogeneous structure of multilayer materials systems allows for a wide variety of tailorable properties, allowing their utilization in a wide field of different engineering systems, *e.g.* thermal barrier coatings [1], microelectronic devices [2] or hard coatings [3] to name a few. However, most of these applications exhibit constituents with micrometer to sub micrometer thicknesses, making the investigation of mechanical response considerably challenging. With the rise of *in situ* micro- and nanomechanical testing techniques, *e.g.* nanoindentation [4,5], microcompression/tension [6,7] or microcantilever bending [8,9], many groups were successful in investigating previously unachievable mechanical parameters of these individual phases. Nevertheless, quantifying interfacial fracture in heterogeneous systems remains a challenge, particular in elastic–plastic systems, where the interplay between plasticity and fracture processes is difficult to distinguish. While fracture mechanical testing techniques in microscopic systems have been established for linear elastic fracture mechanics (LEFM) in homogeneous materials, *e.g.* pillar splitting [10], cantilever bending [11], double cantilever wedging [12], push to pull translation [13] or symmetric double notch testing [14], similar techniques addressing elastic–plastic fracture mechanics (EPFM) have received much less attention [15–17] despite their importance in real engineering systems. Investigations of linear elastic [18,19] or elastic–plastic [20,21] interface failure are even rarer. This is governed by the complex and inseparable relationship between the length scales of multilayer geometries and the prevailing elastic- and plastic deformation fields, which leads to failure modes not otherwise predicted in their homogeneous counterparts. Even in the linear elastic case, the mismatch of elastic properties can lead to, *e.g.* crack deflection [22], acceleration or retardation [23] Hence, considering the additional contribution of varying plastic deformation [24,25] and the influence of loading modes [26,27] results in an even much more intricate problem. However, understanding the local interfacial fracture properties of such systems becomes highly relevant in perspective to macroscopic failure. For example in nacre-like structures the macroscopic fracture toughness is governed by crack deflection along interfaces [28,29]. In blood vessel related medical applications, drug-eluting stents (polymer-coated steels) [30,31] exhibit an extreme amount of plastic deformation through *in vivo* balloon expansion, which can lead to interfacial failure. Aircraft turbines are shielded against high cyclic thermal loadings during their lifetime by thermal barrier coatings, which often start to fail through local debonding at the interface, leading to buckling or full spallation of the coating [32,33]. Finally, microelectronic components can exhibit rather large interfacial stresses through thermal mismatch, either during the deposition process [34,35] or through their lifecycle [36,37], which can lead to failure and consequently a full breakdown of functional properties.

While seemingly from vastly different fields of applications, all of the mentioned cases have in common that their respective failure characteristics originate from a bimaterial interface combination, with at least one plastically deforming component.

There exist methodologies to determine the interface properties of such interfaces given that they interface adhesion is sufficiently weak, *e.g.* indentation buckle delamination [38]. However, such methods are not always applicable and are not able to resolve the actual interplay between plastic deformation and interface fracture. Therefore, to advance the understanding of the underlying processes, given such failure characteristics alternative approaches need to be considered. Furthermore, experimental approaches based on specific lithographic or galvanic microfabricated designs [39,40] could be used to investigate such interface characteristics in a statistical manner. However, such processes could lead to an alteration of the local interface chemistry which can further alter the failure behaviour of the material system [41]. Therefore, methodologies that investigate the specific interface in the native spatially confined state would be beneficial.

The present work aims to establish a better understanding of this generalized kind of problem, focussing on the deformation and fracture along a Cu-WTi interface in a multilayer stack as a model material for microelectronics applications. We utilize *in situ* testing inside a scanning electron microscope (SEM) of electron-transparent specimens using transmission scanning electron microscopy (TSEM). Opposed to scanning transmission electron microscopy (STEM), where a dedicated TEM (typically operated at 200–300 kV acceleration voltage) is used in a scanning configuration, TSEM aims to use a dedicated SEM in a transmission configuration, with the significant benefit of a large chamber for experimental setups and a better contrast generation due to lower acceleration voltages (20–30 kV) [42]. This at the same time comes with the drawback of requiring a rather thin specimen to achieve electron transparency. The specimens are loaded either in a tensile orientation perpendicular to the interface with pre-defined notches to obtain a dominant mode I contribution (opening mode), or in a shear orientation parallel to the interface to obtain a dominant mode II contribution (shearing mode). The automated and continuous collection of images during the experiments allows for a correlation of the sequence of fracture events and accompanying dislocation processes, ultimately providing fundamental insight into the different loading mode-dependent failure mechanisms of elastic–plastic bimaterial interfaces.

2. Experimental procedure

2.1. Material

The multilayer system studied herein consists of an galvanically deposited 5 μm thick Cu layer on top of a 270–300 nm thick single-phase body centred cubic WTi layer (nominally 22 % Ti [43]) with a columnar grain size of approximately 100 nm. These layers are deposited on a single crystalline (001) Si substrate with a 70 nm thermally grown amorphous SiO_x interlayer, as shown in Fig. 1a. The interface between the ductile Cu and the stiff WTi layer exhibits corrugations, while the interfaces between WTi and SiO_x as well as those between SiO_x and Si are almost perfectly flat, as depicted by the red traces in Fig. 1a. For further details on the fabrication of the present material system, the reader is referred to previous works [41,44–46].

2.2. Specimen fabrication

The TSEM deformation experiments were conducted using the experimental approach as described in detail by Stinville *et al.* [47], whereby-two 12 × 10 μm^2 foils with a thickness of 1 μm were processed by focused ion beam milling (FIB, Helios, Thermo Fisher Scientific, Waltham, USA) and lifted onto a pre-processed electronic push-to-pull device (ePTP, Bruker, Billerica, USA) using a micromanipulator needle (OmniProbe, Oxford Instruments, Abington, UK). The specimens were mounted on the device to promote either tensile or shear loading of the interface between Cu and WTi, as shown schematically in Fig. 1b. After manipulating the specimens onto platinum deposited elevations and fixing them with a thick Pt layer to reduce contact compliance [48], subsequent shaping and thinning steps were conducted on the chip with decreasing acceleration voltage and currents down to a minimum of 16 pA at 5 keV, leading to an electron transparent foil used later for either microstructural investigation or micromechanical

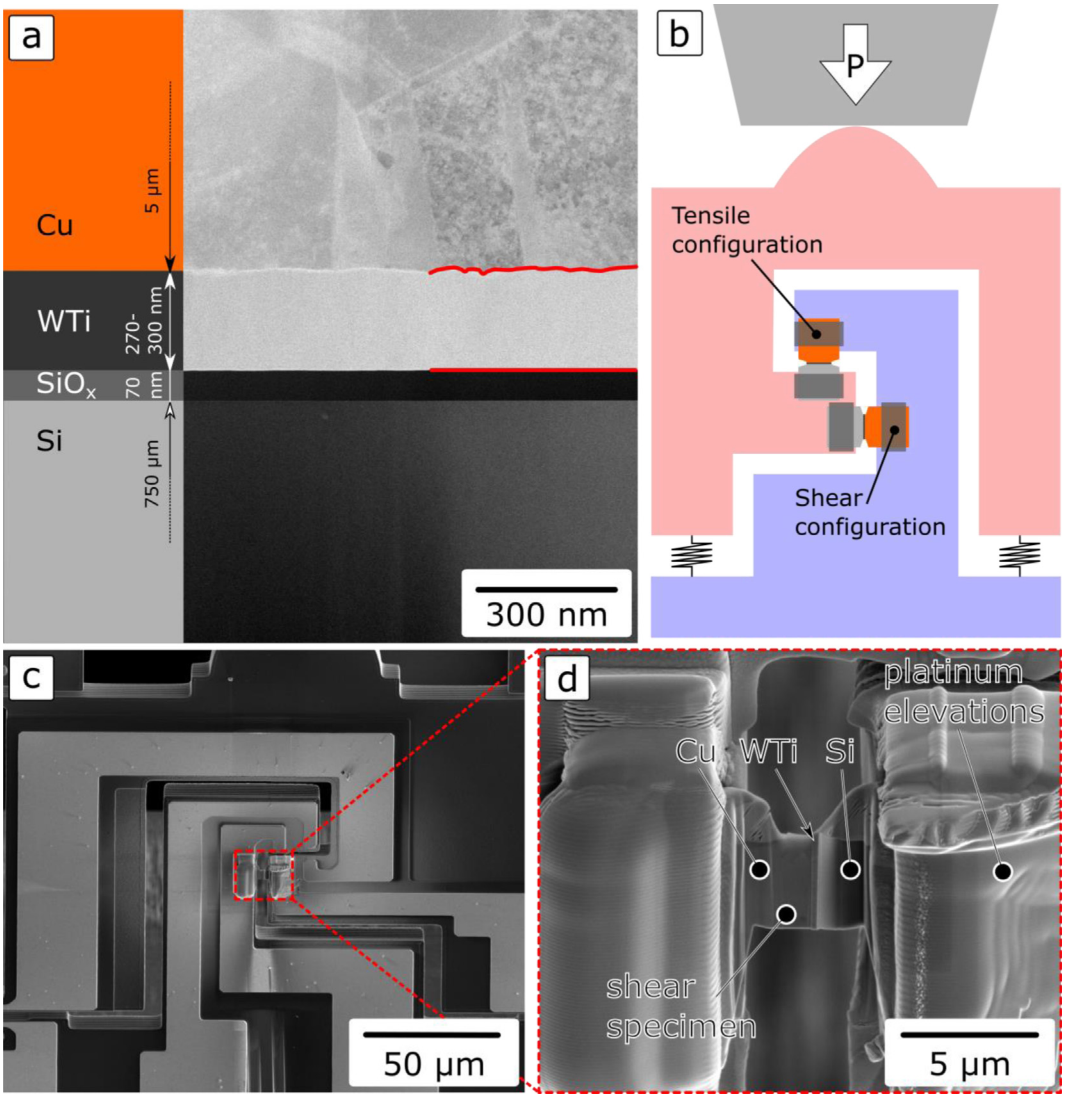

Fig. 1. (a) STEM micrograph of the multi-layered material system showing the individual layers. (b) Schematic of the push to pull device configuration for both, shear and tensile loading. (c,d) SEM images of the shear specimen mounted on the push-to pull device.

testing, respectively. The final shape of the shear specimen before mechanical testing is shown in Fig. 1c and d.

2.3. In situ testing setup

The experiments were conducted *in situ* in an SEM (Apreo S, Thermo Fisher Scientific, Waltham, USA) operated at 30 kV and equipped with an annular STEM detector, which allows the gathering of bright field (BF), annular dark field (ADF) and high angle annular dark field (HAADF) signals through adjustable circular regions of the detector [42]. The ePTP device with the specimen was mounted onto a specifically designed printed circuit board (PCB) adapter piece to fit into a FT-NMT03 nanomechanical testing device (FemtoTools AG, Buchs, Switzerland). This testing device is equipped with a micro electro-mechanical system (MEMS) based load cell with a maximum load of 20 mN and a resolution of $\sim$ 0.1 µN [47]. The experiments were conducted in a closed-loop displacement-controlled manner with a displacement rate of 3 nm/s and a mechanical data acquisition frequency of 100 Hz up to a pre-set maximum load, which was subsequently increased until failure. Lower resolution (LR, 1536x1024 px, 3.26 nm/px) images of all types (BF, ADF, HAADF) were taken continuously with an image acquisition time of 4 s, while higher resolution images (HR, 3072x2048 px, 1.14 nm/px) with image acquisition times of 22 s were taken at consecutive holding segments every 20 s or when load drops larger than 10 µN occurred. The load–displacement data was corrected by the ePTP stiffness k_{ePTP}, as:

$$F_{specimen} = F - k_{ePTP} \cdot u \tag{1}$$

where F and u are the total measured load and displacement and F_{specimen} is the load on the specimen. The ePTP stiffness was measured as the linear slope of the load–displacement data after the specimens were broken.

3. Results

3.1. Tensile loading

To promote failure at the interface of interest (between the Cu and WTi), the specimen was notched prior to thinning by a perpendicular FIB cut as evident in Fig. 2b (initial notch, right-hand side). Through the thinning procedure another notch on the left-hand side was introduced (Fig. 2b, notch from the thinning process), resulting in a double edge notch tension (DENT) geometry with

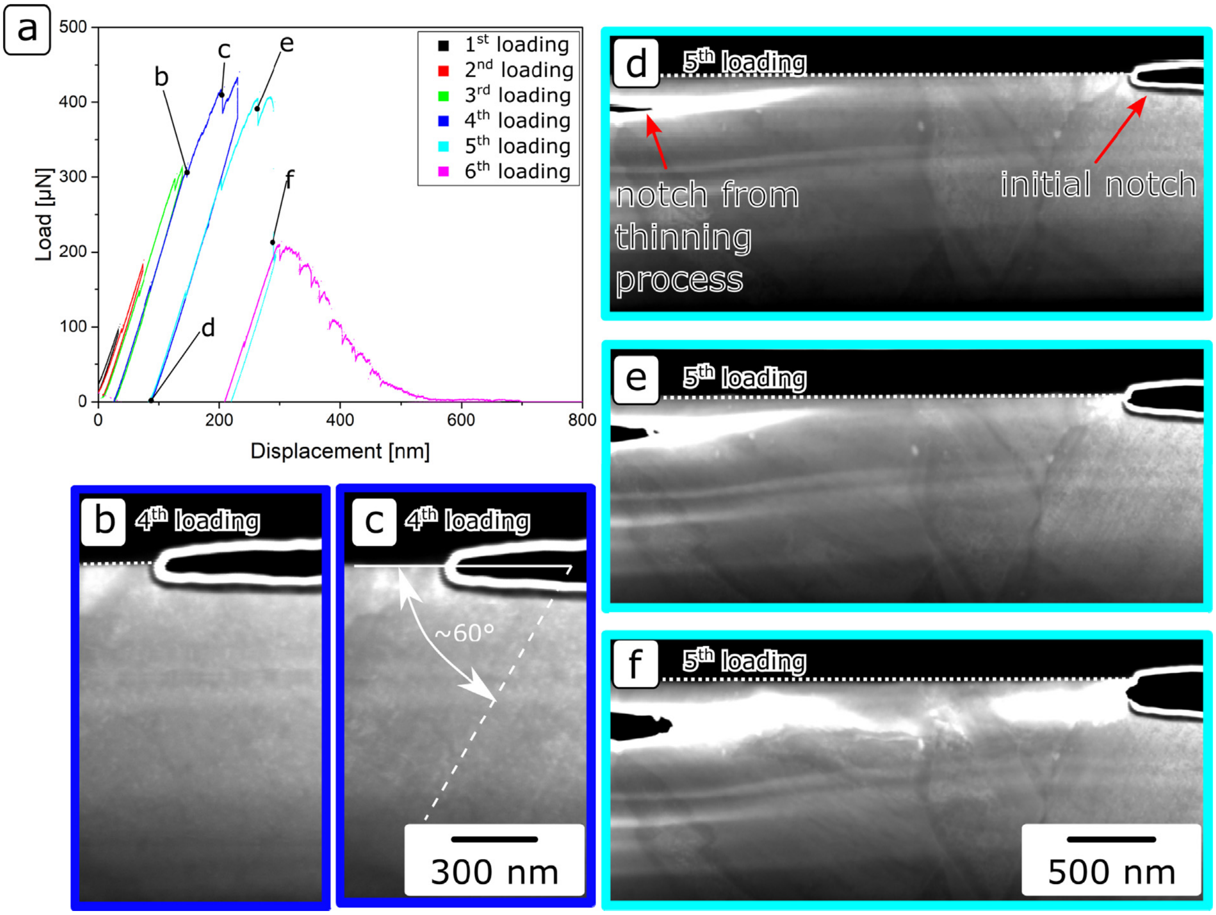

Fig. 2. (a) Tensile specimen load–displacement data of six consecutive loading segments up to final failure. ADF images of the 4th loading step (b) before and (c) after slip traces occur at the predefined notch. ADF images of the 5th loading step (d) in unloaded condition, (e) at the onset of crack tip blunting in the left-hand side notch and (f) after the abrupt load drop showing evident plasticity in front of both notches (bright regions). The dotted lines emphasize the WTi-Cu interface.

the highest stress concentration at the interface. The collected load–displacement data is depicted in Fig. 2a, where the first three loading steps show only a small extent of plasticity. In loading step 4, the first slip traces are evident in the HR images (from Fig. 2b to c) under an angle of about 60° to the notch plane. These slip traces are not confined to a single plane, but fill the Cu grain below the notch, which suggests that either initial dislocations nucleated at the notch tip and cross-slipped within the grain, or the nucleation took place simultaneously at various positions within the FIB induced free surface notch. Subsequent loading (5th loading) leads to obvious crack tip blunting on the left-hand side notch (Fig. 2d to f), as well as nucleation of a crack tip from the right-hand side notch, as shown from Fig. 2d to e. Furthermore, the highly stressed state in front of the right-hand side crack tip is evident by the brighter region in front of it while the contrast and brightness imaging parameters were kept constant, which is a result of local thinning of the specimen through plasticity. Additional loading (Fig. 2e to f) resulted in a significant load drop in conjunction with sudden and massive plastic deformation events in front of both notches, as depicted by the bright regions in Fig. 2f (see supplementary movie). These regions grow together on the Cu side of the specimen, without any crack extension along the WTi-Cu interface, which suggests a lower barrier for plastic deformation in the Cu phase than for interfacial crack extension.

In the 6th loading step, final failure occurred by plastic deformation and crack extension through the Cu phase (see supplementary movie). However, not only the cracks extended, but also separate regions in the interior of the specimen detached before any crack could reach them. For the sake of simplicity, these regions will be called voids in the following, although it is to note that they are in fact two-dimensional holes in a thin foil and not three dimensionally unconnected empty volumes inside the material as commonly assumed in macroscopic fracture analysis [49]. To visualize this process, Fig. 3 depicts multiple LR ADF images of the specimen deformation during 6th loading.

Utilizing an image binarization at a threshold greyscale value of 100 out of 255, the areas corresponding to the two cracks as well as the expanding voids were measured and are visualized on the right-hand side of the corresponding ADF images in Fig. 3. There, it is evident that initial crack tip blunting on both sides is followed by nucleation of voids in the vicinity of the crack tips (Fig. 3b,d). Upon further loading, the left void coalesces with the crack while the right void grows and multiple additional voids nucleate in the specimen interior (Fig. 3e,f). The left-hand side crack continues to grow through void coalescence, while the right-hand side crack exhibits larger crack tip blunting and the interior voids start growing together (Fig. 3g,h). Before all of the voids are connected to one of the two cracks, the remaining interior voids coalesce to one large region (Fig. 3i,j), followed by final failure as both cracks grow together (Fig. 3k,l).

The jagged characteristic of the cracks is most likely due to activation of different slip planes in the individual Cu grains. This is especially evident on the left-hand side crack (Fig. 3e,f) as nearly 90° deviations of the crack flanks are observed, while it is still extending inside a single grain (Fig. 2d).

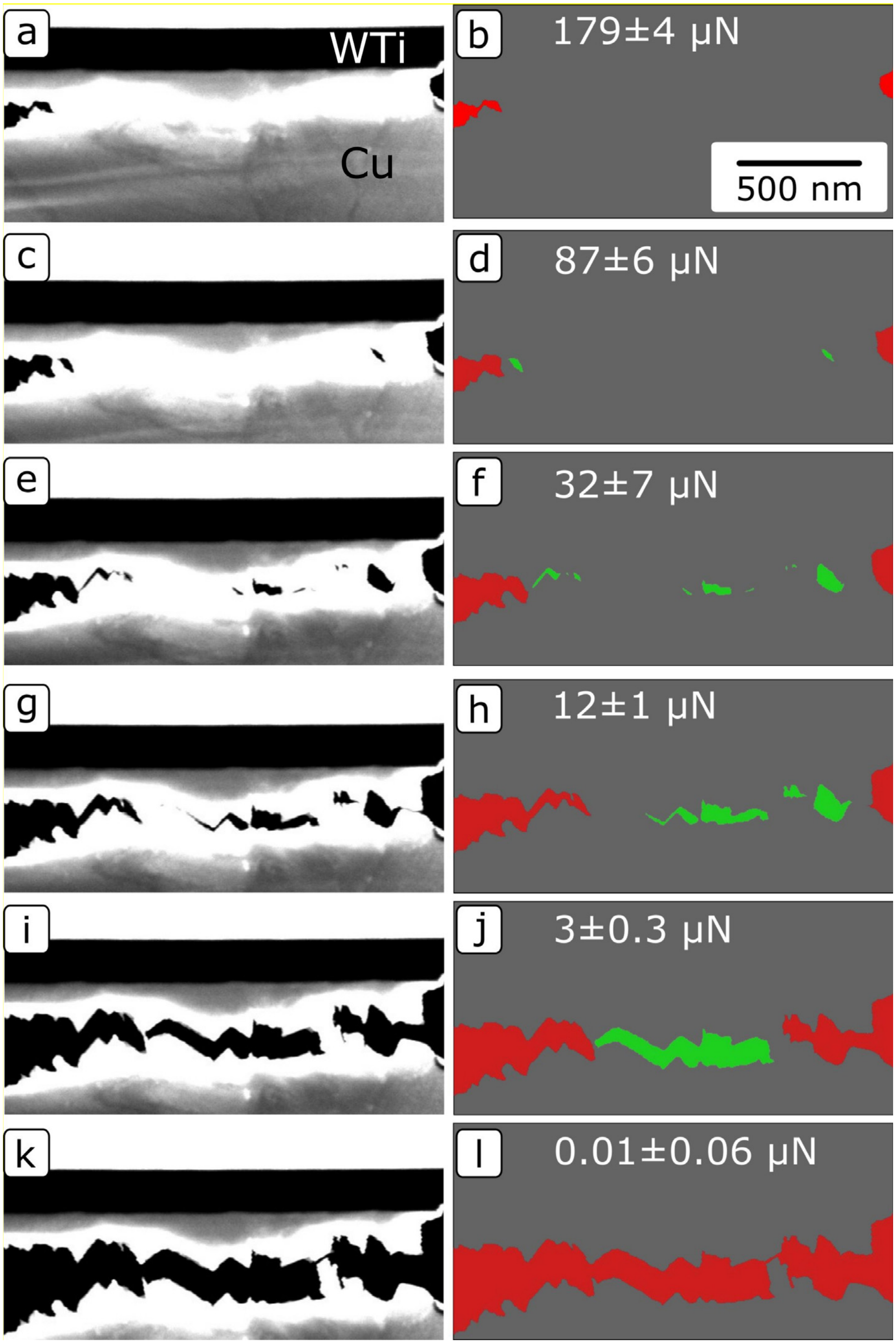

Fig. 3. (a,c,e,g,I,k) Zoomed ADF LR images of loading step 6, showing the growth of the crack by nucleation and coalescence of voids, as well as (b,d,f,h,j,l) the corresponding evaluated crack extension areas and loads, where red areas depict the two cracks and green areas refer to not yet connected voids. The micron bar is applicable to all images.

Fig. 4 shows the combined load–displacement and crack analysis data from the final loading step. The black squares correspond to the average load for each image during the acquisition time with the error bars as standard deviation. The number of voids unconnected to any of the two cracks is shown as blue open circles with the corresponding second axis.

When taking into account the increase of region of interest (ROI) around the two cracks as a function of progressively increasing displacement, one can normalize the measured area of cracks and voids, as:

$$A_{cracks,voids}[-] = \frac{A_{cracks,voids}[px]}{w \cdot h(u)[px]} \tag{2}$$

where $A_{\mathrm{cracks,voids}}$ is the normalized area or area in pixels, w is the constant width of the ROI and h is the increasing height of the ROI as a function of displacement. This increase in height was measured on distinct, non-deforming positions on the LR image away from both cracks and was found to be linear with displacement, which suggests that the full amount of plastic deformation was covered within the ROI.

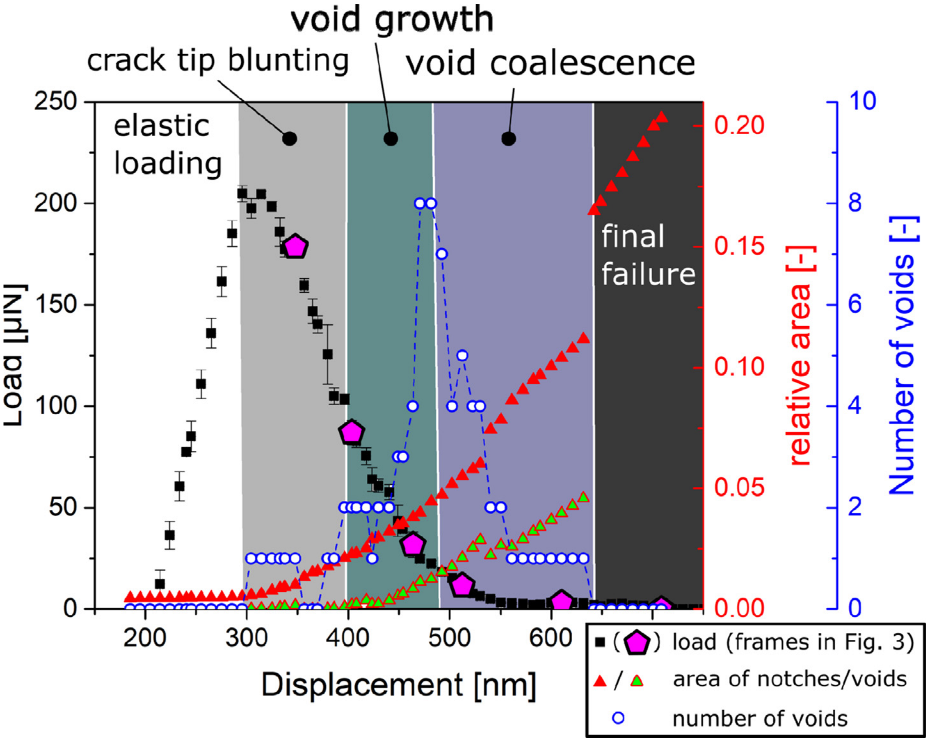

Fig. 4. Load-displacement data (black squares) of the 6th loading step as well as number of interior voids (open blue circles) and relative area of cracks (red triangles) and voids (green filled triangles), respectively. The purple pentagons depict the load level of the ADF LR images as shown in detail in Fig. 3.

The relative area increase of both cracks (filled triangular symbols) as well as voids (green filled triangular symbols) is shown in Fig. 4 as red triangles.

From Fig. 4, five distinct regions are evident. Initially elastic loading took place without any plastic deformation (white region), followed by crack tip blunting on both sides, as shown by the continual increase in crack area (bright grey region). Further loading resulted in void nucleation and growth, as evident in the increase in number of individual voids (pale green region), followed by coalescence of these voids with one of the cracks or with each other, as evident by the decrease of number of voids in conjunction with increase of the void area (pale blue region). Finally, all voids coalesced with one of the cracks up to the complete detachment of both sides of the specimen (dark grey region). While such a behaviour is known to be the primary mechanism in ductile failure from *post mortem* fracture surface analysis [50,51], the present experiment shows this for the first time *in situ* in such a detailed manner.

3.2. Shear loading

3.2.1. Plastic deformation

The second specimen was loaded in a shear configuration (Fig. 1b), to maximize the mode II loading component on the WTi-Cu interface. Fig. 5a shows the load–displacement data of subsequent loading cycles on the specimen and Fig. 5b depicts a BF image of the specimen before loading. The specimen tilt and imaging conditions have been adjusted with a focus on the largest centre grain (grain I), which is bordered by two twinned grains (grain II and V), evident by the straight boundaries between them, two non-twin oriented grains (grain III and IV) and the WTi layer. The first two loading steps showed no evident changes in the images. The first discernible features were evident in loading step 3 between 75 µN and 109 µN (Fig. 5c,d), where parallel straight slip traces occurred from the boundary between grains I and II. These slip traces cover the majority of grain I, suggesting a high density of dislocation sources at the boundary. Furthermore, these slip traces are parallel to the interface between Cu and WTi, which suggests a pure shear loading condition up to this point. The white lines in Fig. 5d depict the projection of all $\langle 1\,1\,0\rangle$ -directions in grain I as calculated from single spot transmission-Kikuchi diffraction measurements, with the red lines depicting the two directions in closest agreement with the observed slip traces. At the next loading step 4 additional slip traces occurred in a direction that deviates from the initial traces (Fig. 5e), suggesting that instead of a pure shear loading, some amount of mixed mode loading with a bending component, is present. The 5th loading step shows a distinctive load drop (Fig. 5a), without any evident changes in the images, which was identified to be the result of breaking of residual platinum, stuck between the two moving parts of the ePTP. Subsequent loading to the maximum of the 5th loading step is shown in Fig. 5f, where both of the previously observed slip trace directions became more prominent, suggesting additional dislocation activity. Furthermore, entangling and piling-up of dislocations in front of the boundary with grain V started to occur. During the 6th loading step, dislocation activity continued, resulting in the formation of two entangled dislocation regions (Fig. 5g), which partially disappeared again upon unloading (see supplementary movie). With increasing deformation and the accompanied crystal rotation, the diffraction condition of grain I became unfavourable to a point where no dislocation activity could be observed (Fig. 5h). However, a contrast changing feature nucleated from the boundary between grains I and II (Fig. 5h), which is most likely a result of local bending of the specimen. Furthermore, during the 7th loading step the Cu detached from the rigid WTi on the right-hand side, leaving a starting crack for the last loading step, which will be analyzed in detail in the next section.

In the beginning of the last (8th) loading step it is evident that the bend contour has not fully vanished (Fig. 5i), even as the ePTP is fully unloaded, which results in a negative loading of the specimen (-175µN). This suggests that the accumulated plastic defor-

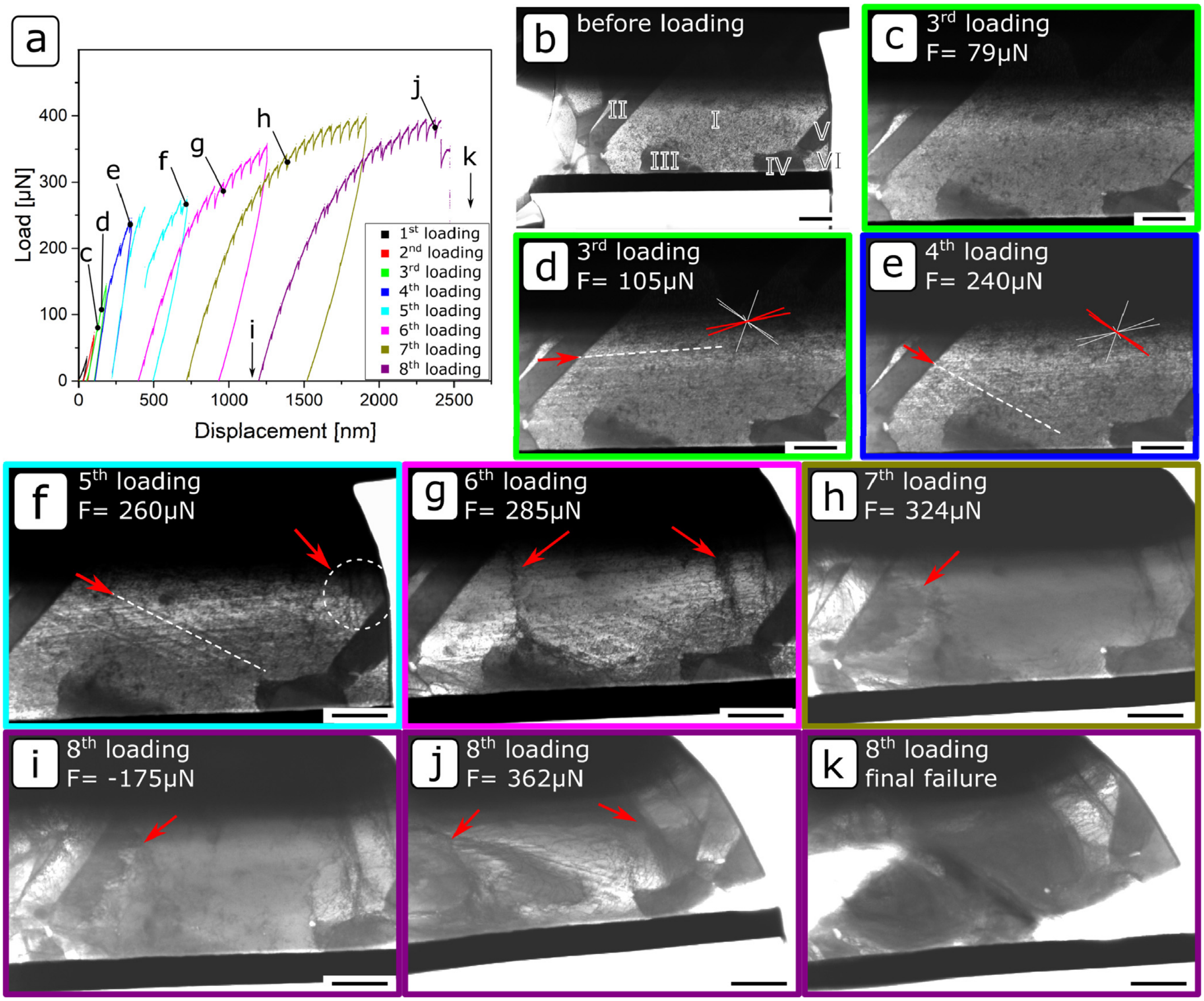

Fig. 5. (a) Shear specimen load–displacement data of eight consecutive loading steps up to final failure. (b) BF image of the specimen before loading with roman numerals (I – VI) depicting individual grains. (c-k) HR BF images of subsequent steps during the experiment. The red arrows depict individual features as described in the text and all micron bars are 500 nm.

mation and resulting residual stresses are high enough to keep the specimen bent locally. Subsequent loading resulted in continuing changes in imaging conditions. However, the two entangled dislocation regions continued to sharpen and form stable sub-grain boundaries (Fig. 5j), as is evident by the different imaging conditions on the right- and left-hand side of the rightmost sub-grain boundary in Fig. 5k. Final failure occurred by sudden nucleation and growth of a second crack from the left-hand side, which resulted in an area of localized plasticity oriented approximately 45° between the two crack tips (Fig. 5k).

With increasing plastic deformation (5th to 8th loading step), a major amount of partially reversible dislocation motion is evident between the loading steps by the deviations between loading and unloading slope (Fig. 5a), as well as the formation and collapse of the local dislocation entanglements (Fig. 5g,h, see supplementary movie).

To assess the local stress situation, we focus on a single dislocation bowing event with respect to increasing load as detailed in Fig. 6. There, sections of the initial five HR BF images during the 6th loading step are shown, zoomed in on a single bowed dislocation. The images were Fourier-filtered to reduce evident mechanical vibration features (see Fig. 6j). Based on the local dislocation radius of curvature R one can estimate the perpendicular shear stress τ acting on the dislocation using the following equation [52–55]:

$$\tau \approx \frac{T}{bR} \approx \frac{Gb^2}{2R} \tag{3}$$

with $T = Gb^2/2$ as the line tension of the dislocation, G = 45 GPa [56] as the shear modulus and b = 256 pm as the Burger's vector (assuming a full $\{111\}\langle 110\rangle$ dislocation). The radius R was calculated as the inverse of the local curvature and the detailed mathematical procedure can be found in appendix A.

It is evident that the curvature of the bowing dislocation decreases with increasing load (Fig. 6a,c,e) to a nearly straight configuration (Fig. 6g) and finally the dislocation unpins and slips away (Fig. 6i). This is also evident in the decreased calculated average shear stress on the dislocation (Fig. 6b,d,f,h). However, some details, such as the direction of the shear stress as well as the actual in-plane position of the dislocation pinning points remain unknown. Two limiting cases can be considered with regards to the pinning point position, namely: (I) a dislocation configuration

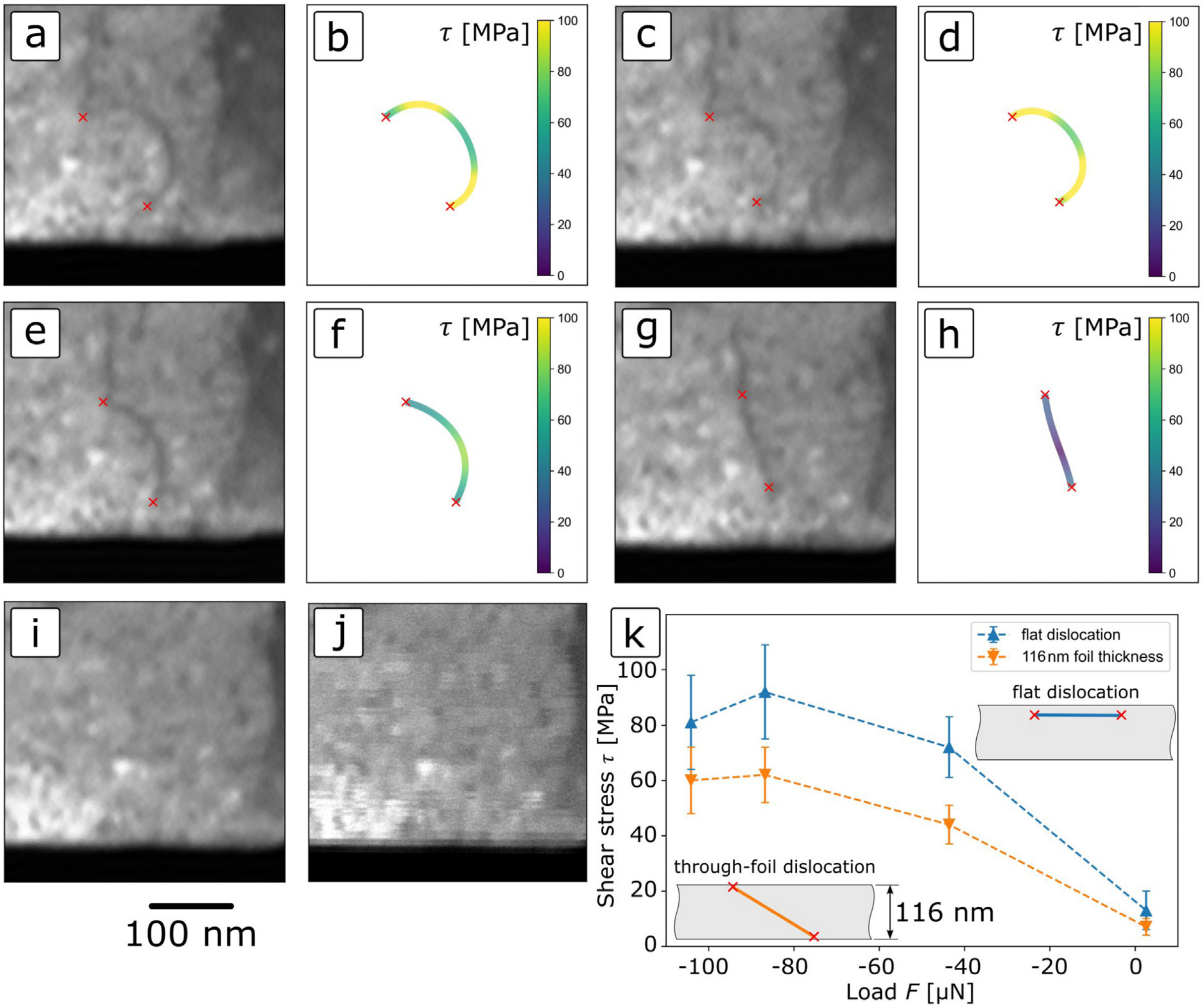

Fig. 6. Fourier-filtered HR BF images and local shear stress as a function of curvature of a single dislocation bow-out at increasing loads: (a,b) −104 µN, (c,d) −87 µN, (e,f) −44 µN, (g,h) 3 µN and (i,j) 49 µN, whereby (j) is the corresponding unfiltered image revealing mechanical vibrations. (k) The calculated shear stress over load for the dislocation being parallel to the image plane (blue, upward pointing triangles) or for an inclined dislocation through a 116 nm thick foil (orange, downward pointing triangles). The micron bar is applicable to images (a-j) and the colorbar depicts shear stress in MPa.

where the whole dislocation line lies perfectly flat in the image plane and is pinned by *e.g.* jogs or other sessile defect configurations (see Fig. 6k, upper right blue dislocation schematic) or (II) a dislocation configuration where one of the pinning points lies on (or very close to) the bottom side of the foil, while the other one lies on the top side of the foil (see Fig. 6k, bottom left orange dislocation schematic).

To address the second case, it is necessary to know the actual foil thickness, which would be only obtainable with additional experiments, *e.g.* electron energy loss spectroscopy or convergent beam electron diffraction. However, based on the fact that the WTi layer is not electron transparent while both the Cu as well as the Si layer are electron transparent, one can estimate an upper bound of the foil thickness based on the inelastic mean free path concept [57–59] as t = 116 nm. The detailed derivation can be found in appendix B.

The shear stress as a function of load is summarized for either of the two extreme cases in Fig. 6k, where the upward pointing, blue triangles correspond to the perfectly flat dislocation and the downward pointing, orange triangles correspond to a ‘through-foil’ dislocation for a maximum foil thickness of 116 nm. The symbols and error bars correspond to the mean value and standard deviation of the center 60 % of the dislocation line, to reduce any artefacts from straight dislocation segments at the pinning points.

3.2.2. Crack extension

During the end of the 7th loading step, at a load of 343 µN, the Cu detached on the right-hand side of the specimen from the WTi layer, initiating an interface crack as depicted in Fig. 7a (red arrow), which grew to a final shape as shown in Fig. 7b at maximum load. Even after unloading to a negative specimen load of −123 µN the interface crack flanks remained separated (Fig. 7c), which suggests a substantial amount of plastic deformation and is in agreement with the details described in the previous section. This allows for a fracture mechanics investigation during the final loading step based on the extension and opening of the initial crack tip, following the well-known 45° construction for the crack tip opening displacement δ [60,61]. However, as the WTi part of the specimen is not subject to plastic deformation the construction is only sensible in one direction. This is shown in Fig. 7e, where the crack length a is measured from the rigid WTi edge perpendicular to the interface to the crack tip, while δ is measured as the perpendicular length between the interface and the intersection of the Cu layer with a 45° construction line.

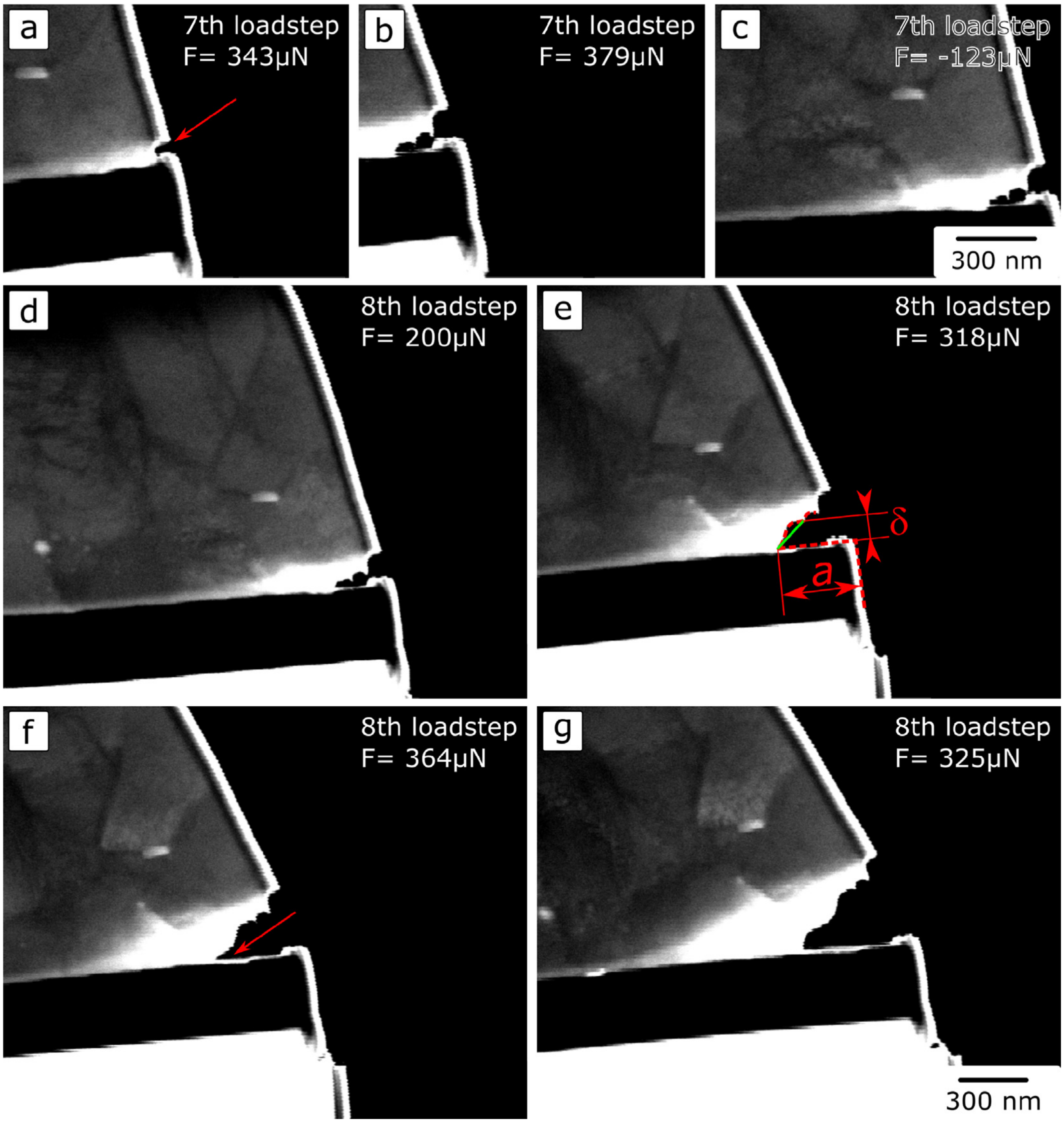

Fig. 7. HR ADF images of (a-c) the 7th loading step showing the initial crack nucleation at the Cu-WTi interface and (d-g) the evolution of the crack during 8th loading step up to final failure. The micron bar in (c) is applicable to all 7th loading step images, while the micron bar in (g) is applicable to all 8th loading step images.

The crack extension during the 8th loading step propagated as follows. Up to quasi-elastic loading (200 μN) the crack remained stable and no change in crack tip geometry was observed (Fig. 7d). Upon further loading the crack opened up considerably, while no major crack extension is evident (Fig. 7e), followed by a faster crack extension regime and a decrease in δ (Fig. 7f, red arrow) as the back part of the Cu layer (presumably a different grain) detached. Thereafter, the crack extension slowed down again, while δ increased up to the final crack tip shape shown in Fig. 7g, which is the last image before final failure.

The resulting δ over a measurements are summarized in Fig. 8, where the positions d-g correspond to the HR ADF images in Fig. 7. The error bars depict a deviation of ± 3 px (±9.8 nm), under the reasonable assumption that the edges can be detected within a 6 px wide margin of error. The dotted line shows a slope of 1.4, which is the suggested value for the construction line in a standardized δ-Δa evaluation following ASTM 1820 [62]. Although this specimen shape deviates considerably from macroscopic standard geometries and ratios, which are boundary conditions for standard evaluation schemes, it indicates that reasonable agreement with macroscopic fracture mechanics is still achieved. The data shows a linear increase of δ with crack extension up to the aforementioned faster crack extension regime (e-f), followed by another linear regime with the same slope up to final failure. Before any of the major failure events occurred δ was in the range of 100 nm, suggesting that the critical crack tip opening displacement δ_c for the interface under the given loading conditions lies in that range.

4. Discussion

The following discussion will highlight the novel insights gained by the present experiments with respect to fracture mechanical considerations, as well as the influence of loading orientation.

4.1. Influence of loading orientation on failure behaviour

The difference in failure mode between the two specimens is evidenced from the fact that, whereas shear loading promotes crack nucleation at the interface between WTi and Cu, tensile loading led to purely ductile failure in the Cu phase. This could have

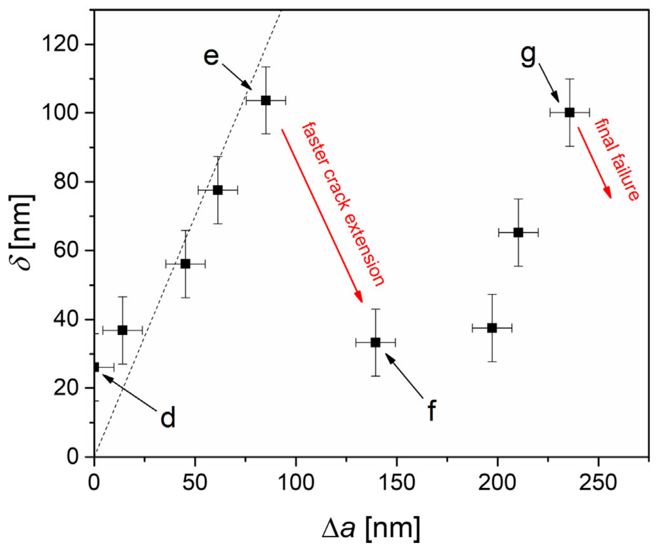

Fig. 8. *Crack tip opening displacement δ over crack extension Δa. The positions d-g correspond to the HR ADF images in Fig. 7 and the dotted line represents a slope of 1.4 as suggested by ASTM 1820 [62].*

multiple reasons, such as the well-established fact that for bimaterial interfaces the external loading mode is not the same as the actual local loading mode at the crack tip [63]. Locally, it is governed by the stresses in front of the crack tip and can be described by the mode mixity angle ψ, as:

$$\psi(r) = \tan^{-1}\left(\frac{\sigma_{xy}(r)}{\sigma_{yy}(r)}\right) \tag{4}$$

for a specific distance r, where σ_{xy} is the shear stress component parallel (corresponding to mode II) and σ_{yy} is the normal stress component perpendicular (corresponding to mode I) in front of the respective crack tip. However, describing ψ analytically is only possible for perfectly linear elastic material behaviour and very specific loading configurations, while still resulting in an oscillatory singularity at the crack tip. In an effort to estimate the mode mixities present in the experiments, finite element simulations (FEM) were conducted based on the actual specimen geometries before the final loading cycle using the freely available CalculiX 2.17 Solver [64], with the assumption of a constant foil thickness of 116 nm and isotropic linear elastic behaviour in the WTi and Si phases. The Cu phase was modelled as elastic-perfectly plastic with a 0.2 % yield onset of 150 MPa [44]. The modelling parameters employed as well as the respective references are summarized in Table 1.

It is emphasized that the results of the given simulations should be taken as qualitative only, as crystallography and three-dimensional specimen thickness were not accounted for and simplified assumptions with regards to deformation were made. Nevertheless, in comparison to each other they provide insight into the differences between the two loading configurations.

Specifically, when comparing the average mode mixity straight in front of the cracks, in a regime between 200 nm and 1000 nm to circumvent any influence of the crack tip singularity, one finds that $\psi_{\text{tensile, left}}$ = 5.9 ± 3.2° and $\psi_{\text{tensile, right}}$ = 5.8 ± 3.6° for the left and right crack tip in the tensile specimen, while ψ_{shear} = 44.7 ± 10.5° for the shear specimen crack tip. This suggests that the tensile specimen is indeed loaded very close to a pure mode I condition ($\psi_{\text{Mode I}}$ = 0°), whereas the shear specimen is not loaded in a pure mode II ($\psi_{\text{Mode II}}$ = 90°) condition, but rather in a mixed mode with equal mode I and mode II contributions. This is further supported by the actual deformed shape of the shear specimen (Fig. 7), where the crack mouth opening displacement (CMOD) evidently increases, which would not be the case for a pure mode II loading.

Table 1
Parameters for the finite element models.

	E **[GPa]**	***ν*** **[-]**	$\boldsymbol{\sigma_y}$ **[MPa]**
Si	160 [65]	0.22 [65]	–
WTi	324 [18]	0.29 [38]	–
Cu	124 [56]	0.35 [56]	150 [44]

However, the pronounced difference in failure characteristics between the two specimens can be explained when investigating the maximum shear stresses in the FEM simulations as shown in Fig. 9. There, the shape of both specimens before the final loading step is shown in conjunction with the maximum shear stress maps in 1:1 matching scale and color schemes for the individual simulations. It is evident that the maximum shear stress is distributed over the majority of the Cu phase in the shear specimen (Fig. 9b), while the tensile specimen only shows very localized maximum shear stress (Fig. 9d). Considering that the shear stress is the main component in driving dislocations, which in turn mediates plasticity, the extent of the maximum shear stress regions can be seen as areas where the majority of non-reversible deformation occurs. While the highest shear stresses arise in the Si and WTi phases of the shear specimen, it is very unlikely to activate any dislocation movement there, as the inherent resistances are considerably higher than in the Cu part. This seems to be in excellent agreement with the previous observations of the shear specimen, where strong dislocation activity was observed in the interior of the Cu grains rather than in the vicinity of the interface (Fig. 5). Even after crack nucleation there was still only very little dislocation movement near the crack tip, while the majority of plastic deformation continued in the specimen interior (Fig. 7). This is again in very good agreement with the FEM simulation, as the maximum shear stress near the crack tip is lower than in the Cu phase (Fig. 9b). The tensile specimen on the other hand shows very localized deformation, and with the exception of some initial slip steps (Fig. 2c), no dislocation activity outside of this region, which again closely resembles the simulation (Fig. 9d), as the maximum shear stress is very localized in this area, suggesting no driving force for any dislocation plasticity outside of it.

4.2. Non-reversible accumulation of plasticity in the shear specimen (Bauschinger effect)

Due to the multiple loading cycles in the plastic regime, not all dislocation activity was completely reversible, as is evident by the formation of dislocation entanglements (Fig. 5g) which remained partially visible even in the unloaded (negative specimen load) state. This, in conjunction with the lower onset of yield in the load displacement data (Fig. 5a) in subsequent cycles, suggests that some of the stored dislocations are pinned only in one direction while being able to move under load reversal. This is commonly referred to as 'Bauschinger effect' [66–68], where initial accumulation of plasticity in one direction lowers the yield onset of subsequent loading in the other direction. This effect is illustrated by the bowed out dislocation in Fig. 6, which was pinned upon unloading at the end of loading step 6. There, the continuous loading during loading step 7 did lead to a decrease of dislocation curvature, which suggests a local shear stress in the opposite direction. Upon reaching positive specimen loads the dislocation did not bow out in the opposite direction, which would be expected if it was fully pinned by, *e.g.* sessile jogs, but it rather slipped away, vanishing out of view. This evident movement of the dislocation happened just on the first occurrence of a positive specimen load, which is usually still considered the elastic regime.

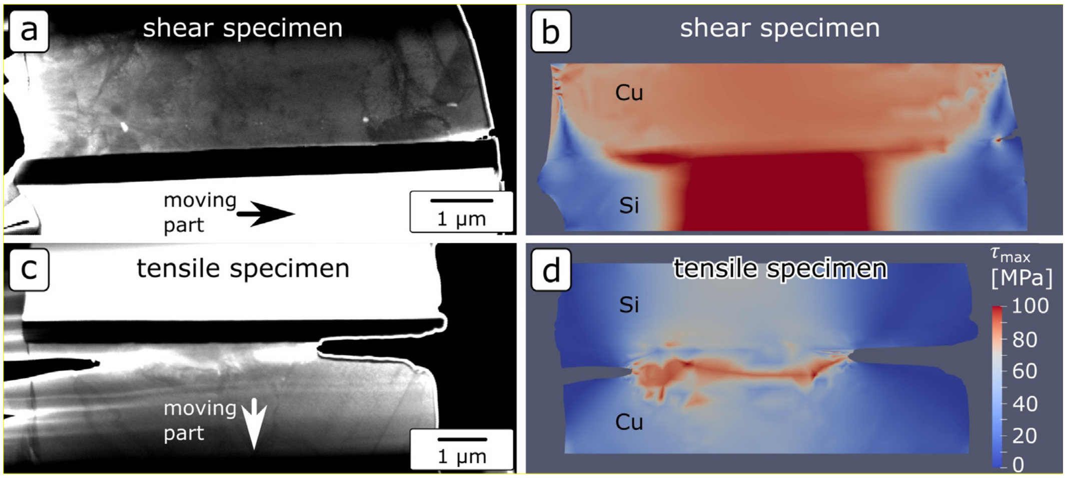

Fig. 9. ADF LR images and maximum shear stress maps from the FEM simulation for (a,b) the shear specimen and (c,d) the tensile specimen. The simulations are scaled 1:1 with the respective images and the colorbar is the same for both of them.

However, due to the previous loading step, non-reversible dislocation mobility was possible.

Comparing this 'Bauschinger effect' between the shear and the tensile specimen, one finds that it is far less pronounced in the latter. This is evident in the load displacement data, which shows no major hysteresis upon reloading for the tensile specimen (Fig. 2a), while pronounced hysteresis effects are visible in the shear specimen from loading step 6 to final failure (Fig. 5a). In conjunction with the FEM simulations this seems reasonable, as the shear stress (Fig. 9d) and resulting plasticity (Fig. 3) are very localized in the tensile specimen, whereas the shear specimen has a quite constant shear stress over a wide area (Fig. 9b), which promotes a larger spatial extent of plastic deformation (Fig. 5). Based on this observation one can argue that cyclic loading conditions with a considerable mode II component, *e.g.* sliding contact in bearings or thermal loading of heterogeneous layered structures, can accommodate a larger amount of defined dislocation structures, *e.g.* persistent slip bands [69–71], than any mode I type experiment would suggest.

4.3. Initial crack nucleation at the interface of the shear specimen

As the deformation of the specimen is governed primarily by plastic slip, the question arises why the interface crack in the shear specimen did nucleate in the first place? In a classical fracture mechanical sense, for such a crack to nucleate the local stress state at the interface needs to be high enough to overcome the interfacial adhesion, which is only possible if little to no dissipating mechanisms, *e.g* dislocation plasticity, are present. One reason for this to occur could be the fact that the detaching grain VI (Fig. 5b) has smaller geometric dimensions than grain I, which shows the most prominent amount of dislocation activity. It is known that smaller dimensions give rise to increased resistance to dislocation glide as:

$$\Delta\tau \sim d^{-m} \tag{5}$$

where $\Delta\tau$ is the increase in necessary shear stress, d is the relevant geometric dimension (most commonly the grain size) and m is a scaling exponent in the range of 0.5–0.66 for fcc materials, depending on whether classical Hall-Petch constraint [72–74] or free standing single crystal investigations [75,76] are considered. Based on the *in situ* observations we observed that the first dislocation activity commenced in two different slip orientations in grain I (Fig. 5d,e), leading to a maximum distance $d_{grain\ \mathrm{I,max}}$ = 3183 nm (from grain II to the right-hand side of grain I) along the first slip trace orientation and $d_{grain\ \mathrm{I,min}}$ = 1671 nm (from grain II to the triple point between grain I, grain IV and the WTi layer) along the second slip trace orientation. Grain VI on the other hand does not show pronounced slip traces, resulting in the absence of a predetermined direction.

However, the largest distance in the whole grain is between the lower left triple junction (grain IV, grain VI and WTi) and the upper right triple junction (grain V, grain VI and vacuum) as $d_{grain\ \mathrm{VI,max}}$ = 573 nm. Thus, utilizing Equation (6), we can estimate that the necessary shear stress to promote dislocation mobility in grain VI is between 1.7 (minimum $d_{grain\ \mathrm{I}}$; m = 0.5) and 3.1 (maximum $d_{grain\ \mathrm{I}}$; m = 0.66) times higher than in grain I, where the majority of dislocation activity was evident. In conjunction with the fact that the local maximum shear stress is considerably less in the vicinity of grain VI than in the specimen interior, as shown in Fig. 9a,b, dislocation activity is considerably hampered in grain VI. This is evident in Fig. 10, where a zoomed section of the specimen is shown focussed on grain VI during the 7th loading step (F = 271 μN), but before the grain rotated out of a favourable imaging condition and the crack nucleated.

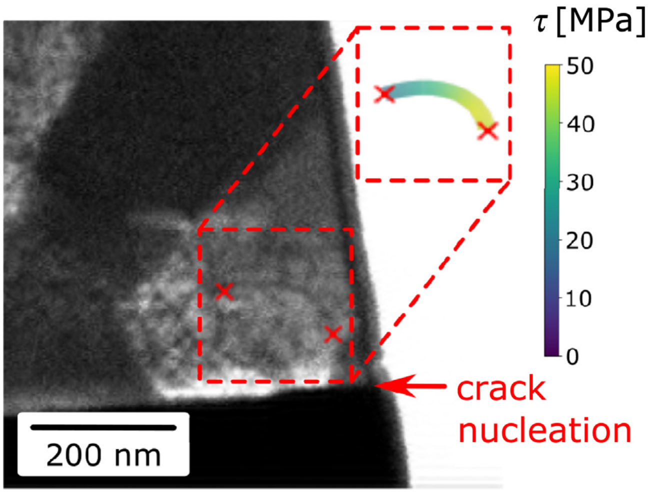

Fig. 10. Zoomed LR BF image focussing on grain VI at the 7th loading step before crack nucleation (F = 271 μN) showing a single dislocation bow-out and quantification of local shear stresses.

While dislocation activity in grain I at such loads occurs via multiple sources of dislocation emission and the build-up of dislocation entanglements (Fig. 5g), the only evident dislocation in the interior of grain VI bows out very slowly and no movement or multiplication of this dislocation is evident up to this point. The average shear stresses (Equation (3), Appendix A) for the given bow-out equates to 51.5 ± 10.6 MPa for a perfectly flat dislocation in the image plane or 39.9 ± 6.1 MPa for a dislocation extending through a 116 nm foil. While there seem to be multiple dislocations in the bottom left triple junction of this grain, no further dislocation mobility was evidenced in the images, which strengthens the argument regarding Hall-Petch [74] hardening.

These points underline that there is only very weak energy dissipation possible via dislocation plasticity in the vicinity of the interface where the crack originated, which results in the energetically favourable opening of the interface and hence a crack originated.

4.4. Details regarding fracture mechanical parameters

Whereas the WTi part of the specimens remains rigid and does not show any evidence of irreversible deformation, the Cu part displays pronounced dislocation activity already before any crack nucleation or crack tip blunting is evident (Fig. 2c, Fig. 5d), regardless of whether the specimens are loaded in shear or tensile direction. As a consequence, a classical linear fracture mechanics quantification of the fracture resistance of the Cu-WTi interface is not viable.

However, considering the onset of dislocation activity-one can estimate a lower bound for the interface fracture resistance. Based on the work of Rice and Thomson [77], Ohr [78] derived an expression for the stress intensity necessary to nucleate an edge dislocation from a crack tip under an angle Φ for mode I loading condition, as:

$$K_{Ie} = \frac{2}{\sin\Phi\cos\frac{\Phi}{2}}\left(\frac{Gb}{(1-\nu)\sqrt{8\pi r_c}} + \sqrt{2\pi r_c}\left(\sigma_y + \frac{4\gamma b \sin\Phi}{\pi {r_c}^2(2+e^3)}\right)\right) \tag{6}$$

where $r_c \approx b$ [52–54] is the dislocation core radius, γ = 1635 mJ/m^2 [79,80] (extrapolated to 25 °C) is taken as the surface energy of Cu and e is Euler's constant. All other variables have been defined previously. Using Φ = 60° as observed in the tensile specimen (Fig. 2c) and σ_y = 150 MPa (see Table 1) the resulting emission stress intensity is estimated as K_{Ie} = 0.75 MPa $\sqrt{m}$. Notably, σ_y has only minor influence on this as the difference between $K_{Ie}(\sigma_y$ = 1 MPa) = 0.74 MPa$\sqrt{m}$ and $K_{Ie}(\sigma_y$ = 400 MPa) = 0.78 MPa$\sqrt{m}$ is only 5.5 %. Furthermore, if considering only the surface energy of W, γ_W = 3500 mJ/m^2 [81], instead of that for Cu, the stress intensity would estimate as K_{Ie} = 0.92 MPa$\sqrt{m}$, resulting in a deviation by 22.3 %. As these are the two species with the lowest and highest surface energies in the vicinity of the interface (Ti lies in between with γ_{Ti} = 1980 mJ/m^2 [82]), the estimated K_{Ie} values can be considered as lower and upper bounds, respectively.

Ohr [78] also discussed the emission of screw dislocations under mode II and mode III loading conditions, which exhibit a lower stress intensity threshold for nucleation, but the necessary plane for dislocation glide would have to be in front of the crack tip parallel to the WTi-Cu interface. As this is clearly not the case and the tensile specimen has a significant mode I component, an argument based on the nucleation of an edge dislocation under mode I seems more sensible.

Furthermore, one can evaluate the tensile experiment as a classical DENT specimen using [83]:

$$K_{DENT} = \frac{F}{Bt}\sqrt{\pi a_0}\,Y\left(\frac{a_0}{B/2}\right) \tag{7}$$

where B = 4995 nm is the specimen width, a_0 = 1119 nm is the (average) initial crack length from one side and $Y(2a_0/B)$ = 1.163 is a geometry factor [83]. With the load corresponding to the first slip trace emerging in the tensile specimen (Fig. 2c) as F = 373 μN and the specimen thickness again as t = 116 nm (aiming for a lower bound), the stress intensity equates to K_{DENT} = 1.40 MPa$\sqrt{m}$, which is about twice as high as the previously calculated K_{Ie}. However, the emission stress intensity calculations consider an atomically sharp crack tip, whereas the actual crack tip has a comparatively large radius of $\rho \approx$ 45 nm (Fig. 2b). Fischer and Beltz [84] have developed a framework for the influence of crack tip radius on the emission stress intensity based, based on Muskhelishvili's complex potential approach [85]. While the full derivation of the equations for the present system is outside the scope of this work, linearly interpolating their data to $\rho/b \approx$ 175 at $a/b \approx$4000 as for the given system leads to a K-value between 2 and 3 times higher than for a sharp notch. This explains the observed discrepancy between K_{Ie} and K_{DENT} and leads to a fairly good agreement.

Hence, one can calculate the J-Integral $J_{DENT} = {K_{DENT}}^2/E_{Cu}$ = 15.8 J/m^2 under the assumption of a plane-stress condition, which is reasonable given the thin specimen. This value is in the range of the J-Integral for the onset of plastic crack tip blunting (between 15.2 and 23.6 J/m^2), measured by the cantilever deflection technique [46]. While the specimen is definitely far outside the realm of classical elastic–plastic fracture mechanical evaluation schemes [62], due to its bi-material nature and confined specimen dimensions in comparison to the plastic zone, similar analysis can still be attempted, in order to obtain a basis for comparison with similar investigations. Considering the first five loading cycles as pre-loading, one can evaluate the J-integral by splitting the individual load hysteresis into elastic and plastic components and calculating the J integral following ASTM 1820 [62]. The resultant data is shown in Fig. 11, where coloured squares correspond to the individual load segments, and an average crack extension measured from both notches using the ADF LR micrographs. Since the last cycle leading to final failure has no unloading slope, *i.e.* no possibility to determine the elastic part of the J-integral, the complete J-integral is estimated using the cohesive zone model approach [86,87], where a traction separation relationship is evaluated through the whole fracture process. The area under this traction-

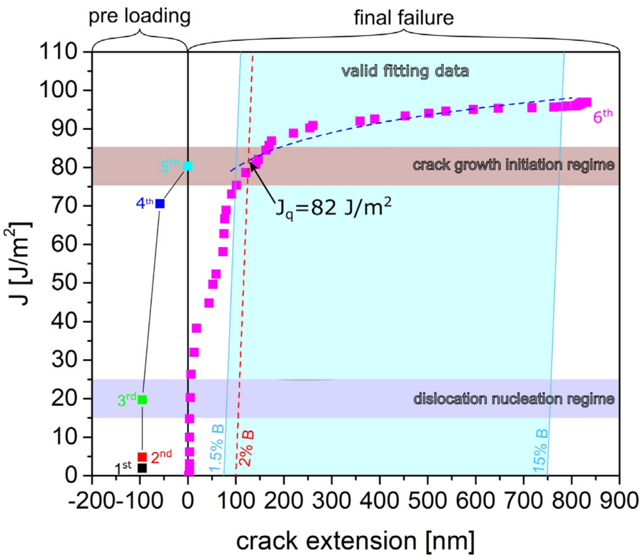

Fig. 11. *J-crack extension data in analogy to classical ASTM 1820 [62] evaluation schemes, considering the first 5 load steps as pre-loading to create a crack.*

separation curve is equivalent to the non-reversible energy [86] of deformation during the process, which we will denote as J_{fracture}, and given the fact that the plastic deformation is rather confined in the ligament between the two cracks (Fig. 3), it can be estimated for the present experiment as [87]:

$$J_{fracture}(u_i) = \frac{1}{(B-2a_0)t}\int_{200nm}^{u_i} F du \tag{8}$$

where u_i is the measured displacement at the i-th frame, the enumeration of which is shown in Fig. 11 over the respective crack extensions measured from the ADF LR micrographs. A slight deviation from a linear blunting slope is evident at a crack extension of approximately 50 nm. This corresponds to a small void of only a couple of pixels which coalesced with the left-hand side notch even before the maximum load was reached. The occurrence of larger voids in front of both crack tips (Fig. 3c,d) occurs at approximately 100 nm and can be considered the end of pure blunting and the start of crack propagation.

In macroscopic evaluation schemes the data between 0.15 mm and 1.5 mm crack extension would be fitted using a $J = c_1 \Delta a^{c_2}$ power law, with c_1, c_2 as fitting parameters, and then the intersection with the 0.2 mm blunting line could be determined. As this is not possible with micron sized specimens, an analogous evaluation procedure was conducted using 1.5 %, 15 % and 2 % of the specimen width B, as suggested by Pippan *et al.* [88], leading to a conditional critical J-integral J_q of 82 J/m^2 (K_{Jq} = 3.19 MPa$\sqrt{\text{m}}$) as shown in detail in Fig. 11. The position of this fitted intersection is in good agreement with the initiation of ductile crack extension by void nucleation as observed during the *in situ* investigations (Fig. 3c,d). Furthermore, J_{fracture} increases only by 20 % to a value of J_{final} = 98 J/m^2 (K_{final} = 3.49 MPa$\sqrt{\text{m}}$) until the last Cu ligament is detached, which suggests that only little energy is plastically dissipated during the fracture process once the crack started to grow.

These values should be taken with some caution, as they describe the whole fracture process based on macroscopic, isotropic and homogeneous assumptions, which are obviously not fulfilled in the present small scale case. Nevertheless, in comparison with the critical fracture toughness of coarse grained (K_{IC} = 88.5 MPa$\sqrt{\text{m}}$), or even ultra-fine grained Cu (K_{IC} = 33.4 MPa$\sqrt{\text{m}}$) in macroscopic experiments [89], our final fracture toughness is still considerably lower. Hirakata *et al.* [90] studied free standing electron beam deposited copper films in the range from 800 nm to 100 nm and found a pronounced size effect in fracture toughness from 7.81 MPa$\sqrt{\text{m}}$ down to 2.34 MPa$\sqrt{\text{m}}$. While their films had a smaller in-plane grain size (369 to 170 nm) than in the present tensile specimen, our fracture toughness values agree rather well, which suggests a major influence of the volumetric constraint on fracture toughness in such thin specimens [91,92]. Therefore, it has to be emphasized that comparison to similar sized specimens is desirable, as association with macroscopic data can lead to incorrect conclusions.

Similar considerations can be outlined for the shear specimen, where the critical crack tip opening displacement at crack extension is estimated to be $\delta_c \approx 100$ nm (Fig. 8). The relationship between J-Integral and crack tip opening displacement in the framework of a Hutchinson-Rice-Rosengreen (HRR) field [93,94] is linear with the proportionality as [61]:

$$J = \frac{\delta \sigma_y}{d(n,\psi)} \tag{9}$$

where $d(n, \psi)$ is a function of the Ramberg-Osgood strain hardening exponent n [95], the mode mixity and of whether a plane strain or plane stress state dominates. Assuming again a majority of plane stress state and aiming for a lower bound ($n \to \infty$), the function $d(n)$ would equal unity without taking the bimaterial nature of the specimen into account (neglecting ψ). Shih *et al.* [96,97] established that $d(n)$ is even higher for a bilayered structure than for a homogenous material. However, they reported only values for distinct mode mixities and plane strain condition. Pirondi and Dalla Donne [98] derived $d(n,\psi)$ based on the HRR field for a homogeneous material, but as a function of mode mixity, and found good agreement with experimental data as well as FE-simulations. Utilizing their data at a mode mixity angle of ψ = 45° results at $d(n, \psi) \approx 1.7$, which equates to J_{shear} = 8.8 J/m^2 for the shear specimen. This is reasonable given the fact that mode II loading results in a lower threshold for crack nucleation given the far field stresses (T-stresses) have a positive contribution to mode I opening [99,100], which is clearly the case considering the large opening angle of the crack tip (Fig. 7g).

While all of the previous considerations are based on simplified assumptions, all arguments were considered towards a lower bound J-integral value, which gives estimates for dislocation nucleation $J_{\text{dislocation}} \approx 15$ J/m^2 and crack extension $J_{\text{crack}} \approx 8.8$ J/m^2. However, while the threshold for fracture seems to be lower, it has to be emphasized that the actual occurrence of crack extension can be strongly influenced by the local chemistry [41] as well as crystallographic orientation relationship. Kysar [101] showed that that the crack along a diffusion bonded single crystal copper-sapphire interface exhibits a slower (ductile) or faster (brittle) crack extension in opposite directions. He found that whether brittle or ductile behaviour occurred was a result of the normal stresses that are able arise in front of the crack tip [102]. Thus, in conjunction with the fact that the dislocation activity in the shear specimen is suppressed by the local stress state (see Fig. 10), this explains the crack extension at a lower J-value, as the local opening stresses overtake the energy dissipation by plasticity.

While the present experiments reveal a deep insight with respect to the interaction between plastic deformation and fracture processes at the interface, it should be emphasized that the gathered quantitative values are distinctive for the given specimens and should not be considered as general fracture parameters. To advance the understanding of such interface failure characteristics it would be beneficial to complement such high-fidelity data, as presented in this work with, easier to obtain, low-fidelity data, *e.g.* indentation buckle delamination [38].

Moving forward from understanding the elastic–plastic fracture processes at bimaterial interfaces towards designing more failure resistant composite materials, there are some general aspects or countermeasures to take along from the present work. Admittedly, the fracture behaviour is strongly influenced by the local stress state and the resulting suppression or enhancement of dislocation plasticity. However, while the local stress state will always depend on external conditions, the suppression of dislocation plasticity is majorly governed by the microstructure, which can be adjusted in certain bounds. Hence, for damage tolerant applications it is recommended to avoid microstructural features that impede dislocation mobility in the vicinity of the interface, *e.g.* high defect densities or small grain sizes, as this will decrease the tendency towards interfacial fracture in such systems.

5. Conclusion

In situ TSEM experiments where conducted on a Cu-WTi-Si-SiO$_x$ multilayer stack with the aim of studying the fracture behaviour of the Cu-WTi interface. Two different loading orientations where investigated to examine the difference between mode I (tensile specimen) and mode II loading (shear specimen) on the failure behaviour of the interface. To the authors' knowledge, this was the first time that a shear configuration was successfully realized on a push-to-shear device in transmission configuration, thereby opening up the field of *in situ* mixed mode fracture investigations in such very confined scales.

While the tensile specimen failed purely by localization of plastic deformation in the Cu phase, the shear specimen exhibited nucleation and further extension of an interface crack after significant plastic deformation in the specimen interior. This can be connected to the local suppression of dislocation activity at the crack tip in shear configuration, both by the local stress state as well as the microstructure in front of the crack tip. Furthermore, it was established that the lower bound for the activation of dislocation plasticity is $J_{\mathrm{dislocation}} \approx 15$ J/m^2, which is in good agreement with previously conducted experiments on the same material system. The threshold for interfacial crack extension in the shear specimen was found to be $J_{\mathrm{crack}} \approx 8.8$ J/m^2, with the caveat that interfacial crack propagation is only possible with a significant mode II component and a local inhibition of dislocation nucleation or propagation. In a broader context, such kind of experiments hold the premise to reveal details regarding plasticity governed fracture processes in systems with a dedicated mixed mode component or common loading conditions with a significant mode II component, as encountered for example in gliding contact in bearings or thermal loading in material systems with different thermal expansion coefficients. In fact, our present work suggests that interfacial failure through crack extension would be inherently localized along the interface, given similar elastic and plastic properties of the constituents. Specifically, for the situation of dislocation plasticity governed metallic materials, this failure could be counteracted by, *e.g.* locally reducing the defect density or increasing the grain size in the vicinity of the interface to reduce dislocation confinement in front of the crack tip. Overall, this paves a strategy towards more damage resistant multiphase structures by topologically optimized microstructures.

Data availability

Data will be made available on request.

Declaration of Competing Interest

The authors declare that they have no known competing financial interests or personal relationships that could have appeared to influence the work reported in this paper.

Acknowledgments

This study was conducted during a research stay at UCSB financed by an Austrian Marshall Plan Scholarship, which is gratefully acknowledged. Further financial support under the scope of the COMET program within the K2 Center "Integrated Computational Material, Process and Product Engineering, IC-MPPE" (Project 859480, A2.12) is also acknowledged. This program is supported by the Austrian Federal Ministries for Transport, Innovation and Technology (BMVIT) and for Digital and Economic Affairs (BMDW), represented by the Österreichische Forschungsförderungsgesellschaft (Funder ID: 10.13039/501100004955), and the federal states of Styria, Upper Austria, and Tyrol. This project has received funding from the European Research Council (ERC) under the European Union's Horizon 2020 research and innovation programme (Grant No. 771146 TOUGHIT). The authors also acknowledge partial support from the NSF MRSEC Program through DMR 1720256 (IRG-1). The research reported here made use of shared facilities of the UCSB MRSEC (NSF DMR 1720256), a member of the Materials Research Facilities Network (www.mrfn.org). GHB acknowledges support from the National Science Foundation Graduate Research Fellowship under Grant No. 1650114. The authors would also like to thank Aidan Taylor, Eric Yao, Jungho (Paul) Shin and Jean-Charles (JC) Stinvillle for support with the experimental setup as well as fruitful discussions.

Data availability

The raw/processed data required to reproduce these findings are available from the corresponding author upon reasonable request.

Appendix A

To determine the stress of a dislocation line segment in three dimensions one needs to calculate the local curvature of the given segment. This can be done by parametrizing the whole dislocation as:

$$\vec{r}(l) = (f(l), g(l), h(l)) \tag{A1}$$

where $f(l)$, $g(l)$ and $h(l)$ are functions of the x,y and z positions of the dislocation in the interval $0 \leq l \leq 1$ (from the beginning to the end of the dislocation line). The functions $f(l)$ and $g(l)$ are 3rd order polynomials fitted to individual points along the dislocation line, while the function $h(t)$ is either 0 (for the case of a flat dislocation) or assumed to be linear through the foil thickness. Utilizing this parametrized form one can calculate a unit tangent $\vec{T}(l)$ as:

$$\vec{T}(l) = \frac{\vec{r}\,'(l)}{\|\vec{r}\,'(l)\|} = \left(\frac{f'(l)}{\|\vec{r}\,'(l)\|}, \frac{g'(l)}{\|\vec{r}\,'(l)\|}, \frac{h'(l)}{\|\vec{r}\,'(l)\|} \right) \tag{A2}$$

where $\vec{r}\,'(l)$ is the first derivative with respect to l and the double bars refer to the Euclidian norm. From this unit tangent $\vec{T}(l)$ the local curvature $\kappa(l)$ is calculated as:

$$\kappa(l) = \frac{1}{R} = \frac{\|\vec{T}\,'(l)\|}{\|\vec{r}\,'(l)\|} \tag{A3}$$

which serves as input for our shear stress estimates (Equation (3)).

Appendix B

The thickness of the foil can be estimated based on the fact that the intensity of the incoming electron beam is reduced by inelastic processes in the material, following a Lambert-Beer type law, as [57,58]:

$$I = I_0 e^{-\frac{t}{\lambda_{inelastic}}} \tag{B1}$$

where I_0 and I are the incoming and outgoing beam intensities, t is the foil thickness and $\lambda_{\mathrm{inelastic}}$ is the inelastic mean free path of an electron in a specific material. The actual transmitted intensity to initial intensity ratio is unknown due to the brightness and contrast adjustments, which lead to a fully saturated detector in vacuum. However, assuming in a worst case scenario that only 1 % of the transmitted intensity is enough to form the gathered images and the fact that the Cu phase is still transparent while the WTi is not, one could argue that the thickness is between 116 nm and 93 nm, as summarized in Table B1. Considering that it is likely that a higher transmitted intensity is necessary for the observed features to be as evident as they are, the foil is probably closer to a thickness of 50 nm, as would be the case for a 10 % transmitted intensity. However, to obtain lower bound values for all mechanical parameters, the higher bound of the foil thickness t = 116 nm was used for calculation.

Table B1
Calculated foil thickness t for occurring species in the specimen and transmission intensities of 1% and 10%.

	$\lambda_{\text{inelastic}}$ (E = 29.7 keV) [nm] [59]	*t (I/I_0 = 1 %)* [nm]	*t (I/I_0 = 10 %)* [nm]
Cu	25.2	116	58
W	20.27	93	47
Ti	28.03	129	65
Si	39.93	184	92

References

[1] J.G. Thakare, C. Pandey, M.M. Mahapatra, R.S. Mulik, Thermal Barrier Coatings - A State of the Art Review, Met. Mater. Int. (2020), https://doi.org/10.1007/s12540-020-00705-w.

[2] Y. Chen, Nanofabrication by electron beam lithography and its applications: A review, Microelectron. Eng. 135 (2015) 57–72, https://doi.org/10.1016/j.mee.2015.02.042.

[3] C. Subramanian, K.N. Strafford, Review of multicomponent and multilayer coatings for tribological applications, Wear. 165 (1993) 85–95, https://doi.org/10.1016/0043-1648(93)90376-w.

[4] J.B. Pethicai, R. Hutchings, W.C. Oliver, Hardness measurement at penetration depths as small as 20 nm, Philos. Mag. A Phys. Condens. Matter, Struct. Defects Mech. Prop. 48 (1983) 593–606, https://doi.org/10.1080/01418618308234914.

[5] G.M. Pharr, An improved technique for determining hardness and elastic modulus using load and displacement sensing indentation experiments, J. Mater. Res. 7 (1992) 1564–1583, https://doi.org/10.1557/JMR.1992.1564.

[6] M.D. Uchic, Sample Dimensions Influence Strength and Crystal Plasticity, Science (80-,) 305 (2004) 986–989, https://doi.org/10.1126/science.1098993.

[7] D. Kiener, W. Grosinger, G. Dehm, R. Pippan, A further step towards an understanding of size-dependent crystal plasticity: In situ tension experiments of miniaturized single-crystal copper samples, Acta Mater. 56 (2008) 580–592, https://doi.org/10.1016/j.actamat.2007.10.015.

[8] D.E.J. Armstrong, A.J. Wilkinson, S.G. Roberts, Measuring anisotropy in Young's modulus of copper using microcantilever testing, J. Mater. Res. 24 (2009) 3268–3276, https://doi.org/10.1557/jmr.2009.0396.

[9] C. Motz, T. Schöberl, R. Pippan, Mechanical properties of micro-sized copper bending beams machined by the focused ion beam technique, Acta Mater. 53 (2005) 4269–4279, https://doi.org/10.1016/j.actamat.2005.05.036.

[10] M. Sebastiani, K.E. Johanns, E.G. Herbert, F. Carassiti, G.M. Pharr, A novel pillar indentation splitting test for measuring fracture toughness of thin ceramic coatings, Philos. Mag. 95 (2015) 1928–1944, https://doi.org/10.1080/14786435.2014.913110.

[11] A. Riedl, R. Daniel, M. Stefenelli, T. Schöberl, O. Kolednik, C. Mitterer, J. Keckes, A novel approach for determining fracture toughness of hard coatings on the micrometer scale, Scr. Mater. 67 (2012) 708–711, https://doi.org/10.1016/j.scriptamat.2012.06.034.

[12] G. Sernicola, T. Giovannini, P. Patel, J.R. Kermode, D.S. Balint, T. Ben Britton, F. Giuliani, In situ stable crack growth at the micron scale, Nat. Commun. 8 (2017) 108, https://doi.org/10.1038/s41467-017-00139-w.

[13] J.J. Schwiedrzik, J. Ast, L. Pethö, X. Maeder, J. Michler, A new push-pull sample design for microscale mode 1 fracture toughness measurements under uniaxial tension, Fatigue Fract. Eng. Mater. Struct. 41 (2018) 991–1001, https://doi.org/10.1111/ffe.12741.

[14] J. Ast, J.J. Schwiedrzik, N. Rohbeck, X. Maeder, J. Michler, Novel micro-scale specimens for mode-dependent fracture testing of brittle materials: A case study on GaAs single crystals, Mater. Des. 193 (2020), https://doi.org/10.1016/j.matdes.2020.108765 108765.

[15] S. Wurster, C. Motz, R. Pippan, Characterization of the fracture toughness of micro-sized tungsten single crystal notched specimen, Philos. Mag. 92 (2012) 1–23, https://doi.org/10.1080/14786435.2012.658449.

[16] J. Ast, B. Merle, K. Durst, M. Göken, Fracture toughness evaluation of NiAl single crystals by microcantilevers - A new continuous J-integral method, J. Mater. Res. 31 (2016) 3786–3794, https://doi.org/10.1557/jmr.2016.393.

[17] M. Alfreider, D. Kozic, O. Kolednik, D. Kiener, In-situ elastic-plastic fracture mechanics on the microscale by means of continuous dynamical testing, Mater. Des. 148 (2018) 177–187, https://doi.org/10.1016/j.matdes.2018.03.051.

[18] K. Matoy, T. Detzel, M. Müller, C. Motz, G. Dehm, Interface fracture properties of thin films studied by using the micro-cantilever deflection technique, Surf. Coatings Technol. 204 (2009) 878–881, https://doi.org/10.1016/j.surfcoat.2009.09.013.

[19] J. Schaufler, C. Schmid, K. Durst, M. Göken, Determination of the interfacial strength and fracture toughness of a-C: H coatings by in-situ microcantilever bending, Thin Solid Films. 522 (2012) 480–484, https://doi.org/10.1016/j.tsf.2012.08.031.

[20] R. Konetschnik, R. Daniel, R. Brunner, D. Kiener, Selective interface toughness measurements of layered thin films, AIP Adv. 7 (2017) 35307, https://doi.org/10.1063/1.4978337.

[21] M. Alfreider, J. Zechner, D. Kiener, Addressing Fracture Properties of Individual Constituents Within a Cu-WTi-SiO_x-Si Multilayer, JOM. (2020), https://doi.org/10.1007/s11837-020-04444-6.

[22] F. Shi, Z. Song, P.N. Ross, G.A. Somorjai, R.O. Ritchie, K. Komvopoulos, Failure mechanisms of single-crystal silicon electrodes in lithium-ion batteries, Nat. Commun. 7 (2016) 11886, https://doi.org/10.1038/ncomms11886.

[23] O. Kolednik, J. Predan, G.X. Shan, N.K. Simha, F.D. Fischer, On the fracture behavior of inhomogeneous materials - A case study for elastically inhomogeneous bimaterials, Int. J. Solids Struct. 42 (2005) 605–620, https://doi.org/10.1016/j.ijsolstr.2004.06.064.

[24] Y. Sugimura, P.G. Lim, C.F. Shih, S. Suresh, Fracture normal to a bimaterial interface: Effects of plasticity on crack-tip shielding and amplification, 43 (n.d.) 1157–1169. doi:10.1016/0956-7151(94)00295-s.

[25] O. Kolednik, The yield stress gradient effect in inhomogeneous materials, Int. J. Solids Struct. 37 (2000) 781–808, https://doi.org/10.1016/S0020-7683(99)00060-8.

[26] K.M. Liechti, Y.S. Chai, Asymmetric Shielding in Interfacial Fracture Under In-Plane Shear, 59 (n.d.) 295–304. doi:10.1115/1.2899520.

[27] N.G. Mathews, A.K. Mishra, B.N. Jaya, Mode dependent evaluation of fracture behaviour using cantilever bending, Theor. Appl. Fract. Mech. 115 (2021), https://doi.org/10.1016/j.tafmec.2021.103069 103069.

[28] U.G.K. Wegst, H. Bai, E. Saiz, A.P. Tomsia, R.O. Ritchie, Bioinspired structural materials, Nat. Mater. 14 (2015) 23–36, https://doi.org/10.1038/nmat4089.

[29] A. Wat, J.I. Lee, C.W. Ryu, B. Gludovatz, J. Kim, A.P. Tomsia, T. Ishikawa, J. Schmitz, A. Meyer, M. Alfreider, D. Kiener, E.S. Park, R.O. Ritchie, Bioinspired nacre-like alumina with a bulk-metallic glass-forming alloy as a compliant phase, Nat. Commun. 10 (2019), https://doi.org/10.1038/s41467-019-08753-6.

[30] K.V. Wolf, Z. Zong, J. Meng, A. Orana, N. Rahbar, K.M. Balss, G. Papandreou, C. A. Maryanoff, W. Soboyejo, An investigation of adhesion in drug-eluting stent layers, J. Biomed. Mater. Res. Part A. 87A (2008) 272–281, https://doi.org/10.1002/jbm.a.31860.

[31] N. Rahbar, K. Wolf, A. Orana, R. Fennimore, Z. Zong, J. Meng, G. Papandreou, C. Maryanoff, W. Soboyejo, Adhesion and interfacial fracture toughness between hard and soft materials, J. Appl. Phys. 104 (2008), https://doi.org/10.1063/1.3021350 103533.

[32] A.G. Evans, D.R. Mumm, J.W. Hutchinson, G.H. Meier, F.S. Pettit, Mechanisms controlling the durability of thermal barrier coatings, Prog. Mater. Sci. 46 (2001) 505–553, https://doi.org/10.1016/S0079-6425(00)00020-7.

[33] M.R. Begley, H.N.G. Wadley, Delamination resistance of thermal barrier coatings containing embedded ductile layers, Acta Mater. 60 (2012) 2497–2508, https://doi.org/10.1016/j.actamat.2011.12.039.

[34] L. Ni, R.M. Pocratsky, M.P. de Boer, Origins of thin film delamination induced by electrodeposition and processing methods to overcome it, Thin Solid Films. 697 (2020), https://doi.org/10.1016/j.tsf.2020.137796 137796.

[35] C. Shang, Y. Wan, J. Selvidge, E. Hughes, R. Herrick, K. Mukherjee, J. Duan, F. Grillot, W.W. Chow, J.E. Bowers, Perspectives on Advances in Quantum Dot Lasers and Integration with Si Photonic Integrated Circuits acsphotonics.1c00707, ACS Photonics. (2021), https://doi.org/10.1021/acsphotonics.1c00707.

[36] M. Nelhiebel, R. Illing, C. Schreiber, S. Wöhlert, S. Lanzerstorfer, M. Ladurner, C. Kadow, S. Decker, D. Dibra, H. Unterwalcher, M. Rogalli, W. Robl, T. Herzig, M. Poschgan, M. Inselsbacher, M. Glavanovics, S. Fraissé, A reliable technology concept for active power cycling to extreme temperatures, Microelectron. Reliab. 51 (2011) 1927–1932, https://doi.org/10.1016/j.microrel.2011.06.042.

[37] R. Darveaux, C. Reichman, N. Islam, Interface Failure in Lead Free Solder Joints, in: 56th Electron. Components Technol. Conf. 2006, IEEE, n.d.: pp. 906–917. doi:10.1109/ECTC.2006.1645763.

[38] A. Kleinbichler, J. Zechner, M.J. Cordill, Buckle induced delamination techniques to measure the adhesion of metal dielectric interfaces, Microelectron. Eng. 167 (2017) 63–68, https://doi.org/10.1016/j.mee.2016.10.020.

[39] S. Gravier, M. Coulombier, A. Safi, N. Andre, A. Boe, J.-P. Raskin, T. Pardoen, New On-Chip Nanomechanical Testing Laboratory - Applications to Aluminum and Polysilicon Thin Films, J. Microelectromechanical Syst. 18 (2009) 555–569, https://doi.org/10.1109/JMEMS.2009.2020380.

[40] F. Saghaeian, J. Keckes, K.A. Schreiber, T. Mittereder, Design and development of MEMS-based structures for in-situ characterization of thermo-mechanical behaviour of thin metal films, Microelectron. Reliab. 88–90 (2018) 829–834, https://doi.org/10.1016/j.microrel.2018.07.005.

[41] M. Alfreider, R. Bodlos, L. Romaner, D. Kiener, The influence of chemistry on the interface toughness in a WTi-Cu system, Acta Mater. (2022), https://doi.org/10.1016/j.actamat.2022.117813 117813.

[42] P.G. Callahan, J.C. Stinville, E.R. Yao, M.P. Echlin, M.S. Titus, M. De Graef, D.S. Gianola, T.M. Pollock, Transmission scanning electron microscopy: Defect observations and image simulations, Ultramicroscopy. 186 (2018) 49–61, https://doi.org/10.1016/j.ultramic.2017.11.004.

[43] C. Kalha, S. Bichelmaier, N.K. Fernando, J.V. Berens, P.K. Thakur, T.-L. Lee, J.J.G. Moreno, S. Mohr, L.E. Ratcliff, M. Reisinger, J. Zechner, M. Nelhiebel, A. Regoutz, Thermal and oxidation stability of Ti_xW_{1-x} diffusion barriers investigated by soft and hard x-ray photoelectron spectroscopy, J. Appl. Phys. 129 (2021), https://doi.org/10.1063/5.0048304 195302.

[44] A. Wimmer, M. Smolka, W. Heinz, T. Detzel, W. Robl, C. Motz, V. Eyert, E. Wimmer, F. Jahnel, R. Treichler, G. Dehm, Temperature dependent transition of intragranular plastic to intergranular brittle failure in electrodeposited Cu micro-tensile samples, Mater. Sci. Eng. A. 618 (2014) 398–405, https://doi.org/10.1016/j.msea.2014.09.029.

[45] S. Bigl, S. Wurster, M.J. Cordill, D. Kiener, Advanced characterisation of thermo-mechanical fatigue mechanisms of different copper film systems for wafer metallizations, Thin Solid Films. 612 (2016) 153–164, https://doi.org/10.1016/j.tsf.2016.05.044.

[46] M. Alfreider, J. Zechner, D. Kiener, Addressing Fracture Properties of Individual Constituents Within a Cu-WTi-SiOx-Si Multilayer, JOM. 72 (2020) 4551–4558, https://doi.org/10.1007/s11837-020-04444-6.

[47] J.C. Stinville, E.R. Yao, P.G. Callahan, J. Shin, F. Wang, M.P. Echlin, T.M. Pollock, D.S. Gianola, Dislocation dynamics in a nickel-based superalloy via in-situ transmission scanning electron microscopy, Acta Mater. 168 (2019) 152–166, https://doi.org/10.1016/j.actamat.2018.12.061.

[48] K.F. Murphy, L.Y. Chen, D.S. Gianola, Effect of organometallic clamp properties on the apparent diversity of tensile response of nanowires, Nanotechnology. 24 (2013), https://doi.org/10.1088/0957-4484/24/23/235704.

[49] J.R. Rice, D.M. Tracey, On the ductile enlargement of voids in triaxial stress fields, J. Mech. Phys. Solids. 17 (1969) 201–217, https://doi.org/10.1016/0022-5096(69)90033-7.

[50] C.O.A. Semprimoschnig, J. Stampfl, R. Pippan, O. Kolednik, A NEW POWERFUL TOOL FOR SURVEYING CLEAVAGE FRACTURE SURFACES, Fatigue Fract. Eng. Mater. Struct. 20 (1997) 1541–1550, https://doi.org/10.1111/j.1460-2695.1997.tb01509.x.

[51] G. Hutiu, V.-F. Duma, D. Demian, A. Bradu, A. Podoleanu, Assessment of Ductile, Brittle, and Fatigue Fractures of Metals Using Optical Coherence Tomography, Metals (Basel). 8 (2018) 117, https://doi.org/10.3390/met8020117.

[52] A.S. Argon, Strenghtening mechanisms in crystal plasticity, Oxford University Press, n.d.

[53] D. Hull, D.J. Bacon, Introduction to Dislocations, Elsevier (2011), https://doi.org/10.1016/C2009-0-64358-0.

[54] J.P. Hirth, J. Lothe, Theory of Dislocations, Wiley & Sons, 1983.

[55] F. Mompiou, M. Legros, A. Sedlmayr, D.S. Gianola, D. Caillard, O. Kraft, Source-based strengthening of sub-micrometer Al fibers, Acta Mater. 60 (2012) 977–983, https://doi.org/10.1016/j.actamat.2011.11.005.

[56] H.M. Ledbetter, E.R. Naimon, Elastic Properties of Metals and Alloys. {II}. Copper, 3 (n.d.) 897–935. doi:10.1063/1.3253150.

[57] D.B. Williams, C.B. Carter, Transmission electron microscopy: A textbook for materials science, Springer (2009), https://doi.org/10.1007/978-0-387-76501-3.

[58] M. Fox, Optical Properties of Solids, Oxford University Press, 2010.

[59] H. Shinotsuka, S. Tanuma, C.J. Powell, D.R. Penn, Calculations of electron inelastic mean free paths. X. Data for 41 elemental solids over the 50 eV to 200 keV range with the relativistic full Penn algorithm, Surf. Interface Anal. 47 (2015) 1132, https://doi.org/10.1002/sia.5861.

[60] D.M. Tracey, Finite Element Solutions for Crack-Tip Behavior in Small-Scale Yielding, J. Eng. Mater. Technol. 98 (1976) 146–151, https://doi.org/10.1115/1.3443357.

[61] C.F. Shih, Relationships between the J-integral and the crack opening displacement for stationary and extending cracks, J. Mech. Phys. Solids. 29 (1981) 305–326, https://doi.org/10.1016/0022-5096(81)90003-X.

[62] ASTM Standard E1820, Standard Test Method for Measurement of Fracture Toughness, West Conshohocken, USA, USA, 2013. doi:10.1520/E1820-13. Copyright.

[63] J.W. Hutchinson, Z. Suo, Mixed Mode Cracking in Layered Materials, in: Adv. Appl. Mech., Elsevier, 1991: pp. 63–191. doi:10.1016/S0065-2156(08)70164-9.

[64] G. Dhondt, The Finite Element Method for Three-Dimensional Thermomechanical Applications, John Wiley & Sons Ltd, Chichester, UK (2004), https://doi.org/10.1002/0470021217.

[65] M.A. Hopcroft, W.D. Nix, T.W. Kenny, What is the Young's modulus of silicon?, J Microelectromechanical Syst. 19 (2010) 229–238, https://doi.org/10.1109/JMEMS.2009.2039697.

[66] E. Demir, D. Raabe, Mechanical and microstructural single-crystal Bauschinger effects: Observation of reversible plasticity in copper during bending, 58 (n.d.) 6055–6063. doi:10.1016/j.actamat.2010.07.023.

[67] M.W. Kapp, C. Kirchlechner, R. Pippan, G. Dehm, Importance of dislocation pile-ups on the mechanical properties and the Bauschinger effect in microcantilevers, J. Mater. Res. 30 (2015) 791–797, https://doi.org/10.1557/jmr.2015.49.

[68] J. Rajagopalan, C. Rentenberger, H.P. Karnthaler, G. Dehm, M.T.A. Saif, In situ TEM study of microplasticity and Bauschinger effect in nanocrystalline metals, Acta Mater. 58 (2010) 4772–4782, https://doi.org/10.1016/j.actamat.2010.05.013.

[69] E.E. Laufer, W.N. Roberts, Dislocations and persistent slip bands in fatigued copper, Philos. Mag. A J. Theor. Exp. Appl. Phys. 14 (1966) 65–78, https://doi.org/10.1080/14786436608218989.

[70] P. Lukáš, M. Klesnil, J. Krejčí, Dislocations and Persistent Slip Bands in Copper Single Crystals Fatigued at Low Stress Amplitude, Phys. Status Solidi. 27 (1968) 545–558, https://doi.org/10.1002/pssb.19680270212.

[71] D. Kuhlmann-Wilsdorf, C. Laird, Dislocation behavior in fatigue, Mater. Sci. Eng. 27 (1977) 137–156, https://doi.org/10.1016/0025-5416(77)90166-5.

[72] E.O. Hall, The deformation and ageing of mild steel: III discussion and results, 64 (n.d.) 747–753.

[73] N.J. Petch, The cleavage strength of polycrystals, J. Iron Steel InstInst. 174 (1953) 25–28.

[74] E. Arzt, Size effects in materials due to microstructural and dimensional constraints: A comparative review, Acta Mater. 46 (1998) 5611–5626, https://doi.org/10.1016/S1359-6454(98)00231-6.

[75] R. Dou, B. Derby, A universal scaling law for the strength of metal micropillars and nanowires, Scr. Mater. 61 (2009) 524–527, https://doi.org/10.1016/j.scriptamat.2009.05.012.

[76] M.D. Uchic, P.A. Shade, D.M. Dimiduk, Micro-compression testing of fcc metals: A selected overview of experiments and simulations, Jom. 61 (2009) 36–41, https://doi.org/10.1007/s11837-009-0038-2.

[77] J.R. Rice, R. Thomson, Ductile versus brittle behaviour of crystals, 29 (n.d.) 73–97. doi:10.1080/14786437408213555.

[78] S.M. Ohr, An electron microscope study of crack tip deformation and its impact on the dislocation theory of fracture, 72 (n.d.) 1–35. doi:10.1016/0025-5416(85)90064-3.

[79] V.K. Kumykov, I.N. Sergeev, V.A. Sozaev, M.V. Gedgagova, Surface tension of copper in solid phase, Bull. Russ. Acad. Sci. Phys. 81 (2017) 357–359, https://doi.org/10.3103/s1062873817030236.

[80] V.K. Kumykov, V.A. Sozaev, Z.K. Abazova, M.V. Gedgagova, Measuring the Temperature Coefficient of the Surface Tension of Metals in the Solid State, Bull. Russ. Acad. Sci. Phys. 82 (2018) 817–819, https://doi.org/10.3103/s1062873818070286.

[81] D. Scheiber, O. Renk, M. Popov, L. Romaner, Temperature dependence of surface and grain boundary energies from first principles, Phys. Rev. B. 101 (2020), https://doi.org/10.1103/PhysRevB.101.174103 174103.

[82] T.A. Roth, P. Suppayak, The surface and grain boundary free energies of pure titanium and the titanium alloy Ti–6Al–4V, Mater. Sci. Eng. 35 (1978) 187–196, https://doi.org/10.1016/0025-5416(78)90120-9.

[83] H. Tada, A. Press, P.C. Paris, Stress Analysis of Cracks Handbook, ASME Press, n.d.

[84] L.L. Fischer, G.E. Beltz, The effect of crack blunting on the competition between dislocation nucleation and cleavage, J. Mech. Phys. Solids. 49 (2001) 635–654, https://doi.org/10.1016/s0022-5096(00)00042-9.

[85] N.I. Muskhelishvili, Basic Equations of the Plane Theory of Elasticity, in: Some Basic Probl. Math. Theory Elast., Springer Netherlands, 1977: pp. 89–104. doi:10.1007/978-94-017-3034-1_4.

[86] M. Elices, G.V. Guinea, J. Gómez, J. Planas, The cohesive zone model: advantages, limitations and challenges, Eng. Fract. Mech. 69 (2002) 137–163, https://doi.org/10.1016/S0013-7944(01)00083-2.

[87] J. Zechner, M. Janko, O. Kolednik, Determining the fracture resistance of thin sheet fiber composites – Paper as a model material, Compos. Sci. Technol. 74 (2013) 43–51, https://doi.org/10.1016/j.compscitech.2012.10.007.

[88] R. Pippan, S. Wurster, D. Kiener, Fracture mechanics of micro samples: Fundamental considerations, Mater. Des. 159 (2018) 252–267, https://doi.org/10.1016/j.matdes.2018.09.004.

[89] A. Hohenwarter, R. Pippan, A comprehensive study on the damage tolerance of ultrafine-grained copper, Mater. Sci. Eng. A. 540 (2012) 89–96, https://doi.org/10.1016/j.msea.2012.01.089.

[90] H. Hirakata, O. Nishijima, N. Fukuhara, T. Kondo, A. Yonezu, K. Minoshima, Size effect on fracture toughness of freestanding copper nano-films, Mater. Sci. Eng. A. 528 (2011) 8120–8127, https://doi.org/10.1016/j.msea.2011.07.071.

[91] E.I. Preiß, B. Merle, M. Göken, Understanding the extremely low fracture toughness of freestanding gold thin films by in-situ bulge testing in an AFM, Mater. Sci. Eng. A. 691 (2017) 218–225, https://doi.org/10.1016/j.msea.2017.03.037.

[92] R. Qu, R. Maaß, Z. Liu, D. Tönnies, L. Tian, R.O. Ritchie, Z. Zhang, C.A. Volkert, Flaw-insensitive fracture of a micrometer-sized brittle metallic glass, Acta Mater. 218 (2021), https://doi.org/10.1016/j.actamat.2021.117219 117219.

[93] J.W. Hutchinson, Singular behaviour at the end of a tensile crack in a hardening material, J. Mech. Phys. Solids. 16 (1968) 13–31, https://doi.org/10.1016/0022-5096(68)90014-8.

[94] J.R. Rice, G.F. Rosengren, Plane strain deformation near a crack tip in a power-law hardening material, J. Mech. Phys. Solids. 16 (1968) 1–12, https://doi.org/10.1016/0022-5096(68)90013-6.

[95] W. Ramberg, W.R. Osgood, Description of stress-strain curves by three parameters, 1943. http://hdl.handle.net/2060/19930081614.

[96] C.F. Shih, R.J. Asaro, N.P. O'Dowd, Elastic-Plastic Analysis of Cracks on Bimaterial Interfaces: Part III - Large-Scale Yielding, J. Appl. Mech. 58 (1991) 450–463, https://doi.org/10.1115/1.2897206.

[97] C.F. Shih, Cracks on bimaterial interfaces: elasticity and plasticity aspects, Mater. Sci. Eng. A. 143 (1991) 77–90, https://doi.org/10.1016/0921-5093(91)90727-5.

[98] A. Pirondi, C.D. Donne, Characterisation of ductile mixed-mode fracture with the crack-tip displacement vector, Eng. Fract. Mech. 68 (2001) 1385–1402, https://doi.org/10.1016/s0013-7944(01)00023-6.

[99] D. Smith, M. Ayatollahi, M. Pavier, On the consequences of T-stress in elastic brittle fracture, Proc. R. Soc. A Math. Phys, Eng. Sci. 462 (2006) 2415–2437, https://doi.org/10.1098/rspa.2005.1639.

[100] M.R. Ayatollahi, M.R.M. Aliha, On determination of mode II fracture toughness using semi-circular bend specimen, Int. J. Solids Struct. 43 (2006) 5217–5227, https://doi.org/10.1016/j.ijsolstr.2005.07.049.

[101] J.W. Kysar, Directional dependence of fracture in copper/sapphire bicrystal, Acta Mater. 48 (2000) 3509–3524, https://doi.org/10.1016/S1359-6454(00)00127-0.

[102] J.W. Kysar, Continuum simulations of directional dependence of crack growth along a copper/sapphire bicrystal interface. Part II: Crack tip stress/deformation analysis, J. Mech. Phys. Solids. 49 (2001) 1129–1153, https://doi.org/10.1016/S0022-5096(00)00071-5.